Swell Generation Under Extra-Tropical Storms

M. C. Hell[1] , Alex Ayet[2,3] , and Bertrand Chapron[4]

[1]Scripps Institution of Oceanography, University of California San Diego, La Jolla, CA, USA, [2]Climat, Environnement, Couplages, Incertitudes, CECI, Université de Toulouse, CNRS, CERFACS, Toulouse, France, [3]CNRM, Université de Toulouse, Météo-France, CNRS, Toulouse, France, [4]Ifremer, CNRS, IRD, Univ. Brest/ Laboratoire d'Océanographie Physique et Spatiale (LOPS), IUEM, Brest, France

Abstract Storms propagate over the ocean and create moving patches of strong winds that generate swell systems. Here, we describe the dynamics of wave generation under a moving storm by using a simple parametric model of wave development, forced by a temporally and spatially varying moving wind field. This framework reveals how surface winds under moving storms determine the origin and amplitude of swell events. Swell systems are expected to originate from locations different than the moving high-wind forcing regions. This is confirmed by a physically informed optimization method that back-triangulates the common source locations of swell using their dispersion slopes, simultaneously measured at five wave-buoy locations. Hence, the parametric moving fetch model forced with reanalysis winds can predict the displacement between the highest winds and the observed swell source area. The model further shows that the storm's peak wind speed is the key factor determining swell energy since it determines surface wind gradients that lead to the spatial convergence of wave energy into a much smaller area than the wind fetch. Swell generation can then be described to follow a three-stage process that outlines a focus area where swell energy is enhanced and slightly displaced from the maximum wind locations. This analysis provides an improved understanding of fetches for extra-tropical swell systems and may help to identify biases in swell forecast models, air-sea fluxes, and upper-ocean mixing estimations.

Plain Language Summary Storms generate waves on the ocean surface that can travel across entire ocean basins, the so-called swell waves. However, it is unclear how the amplitude and period of these surface waves depend on the strength and shape of the storm. One has to consider the movement of the storm in addition to its size, lifetime, and wind speeds. This study shows how all these parameters control the amplitude and period of swell events reaching the coastlines. We find that the storm's movement and its peak wind speed compress the wave energy to a small area, which then appears as a swell source location in the open ocean. This study can help to improve swell forecasts and understand how long-term changes in mid-latitude storms would modify the exchange of momentum and heat between the atmosphere and the ocean.

1. Introduction

Swell events are long-crested linear wave systems that propagate across the ocean basins (Ardhuin et al., 2009; Munk & Snodgrass, 1957; Snodgrass et al., 1966). Swells impact harbor safety, coastal floating, and beach erosion (Enríquez et al., 2017; Ferreira, 2005; Hunt, 1961; Morison & Imberger, 1992; Russell, 1993; Wilson, 1957), but also modulate sea surface height and affect altimeter and other remote sensing observations (like future SWOT or ICESat-2, Morrow et al., 2019; Klotz et al., 2020). Importantly, swells play a role in air-sea interactions, possibly altering the sea surface roughness and subsequent turbulent air-sea fluxes (Makin, 2008). In addition, swell systems trace intense air-sea exchanges, and hence can potentially help to better understand air-sea fluxes and mixed-layer variability under storms, as well as impacts on global climate. The motivation of this study is to provide rapid and robust means for describing swell generation and how swell events are driven by mid-latitude storm variability.

Swell waves are routinely observed, for example, along coastlines using the Coastal Data Information Program/National Data Buoy Center (CDIP/NDBC, O'Reilly et al., 2016, Figures 1b–1e), or from space by Synthetic Aperture Radar (SAR) images (Chapron et al., 2001) and Real Aperture Radar measurements (Hauser et al., 2020). These observations can be used to back-track swell to focal points or swell source locations,
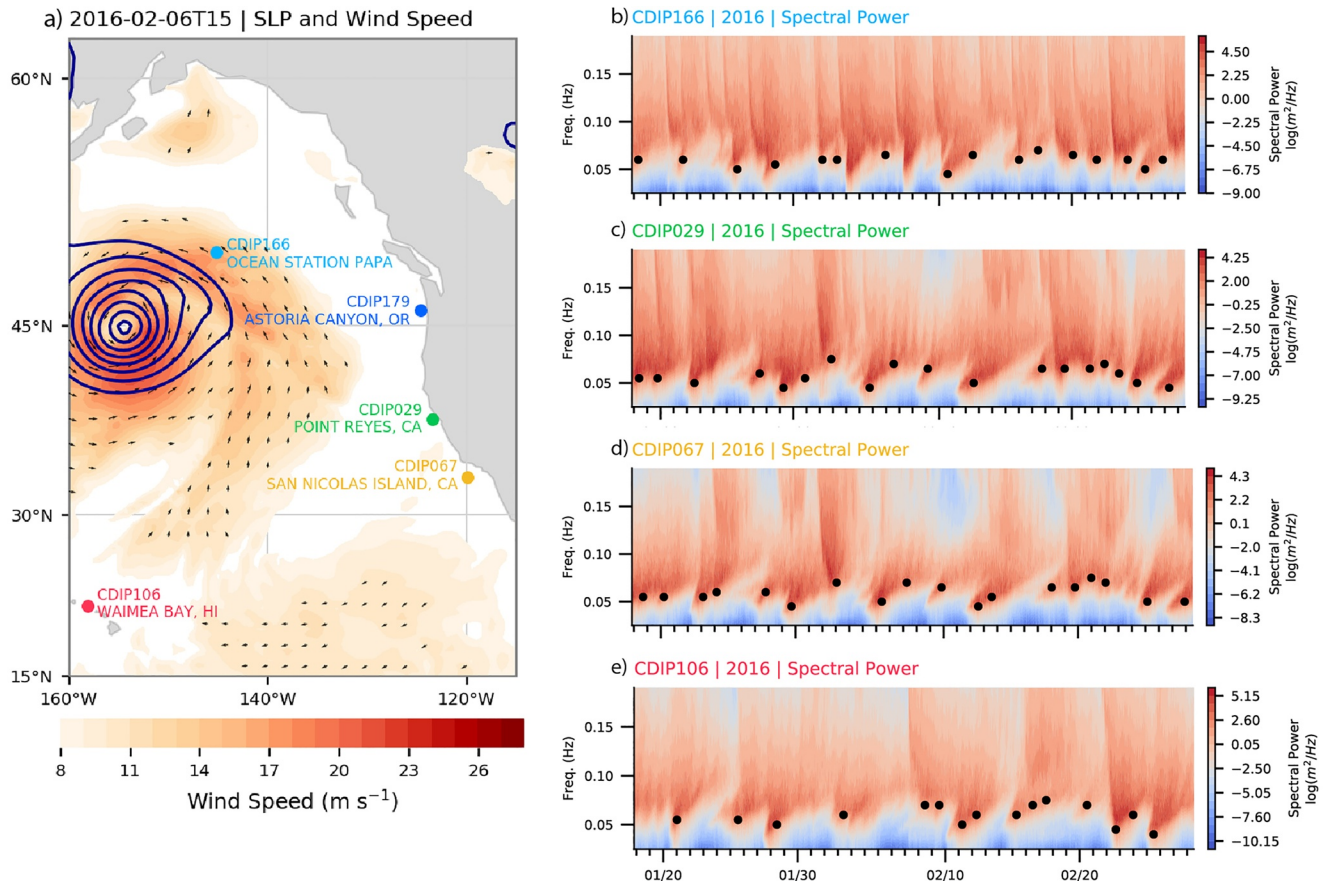
Figure 1. (a) Example synoptic situation on February 2, 2016 with the surface wind speed (shading) and negative anomalies of sea level pressure (SLP) in dark blue with 5 hPa increments. The arrows indicate the surface wind direction and intensity. The position of the CDIP wave buoy stations in panel b to e are shown as colored dots. The 10-m winds and SLP fields are taken from the hourly ERA5 analysis on a 0.25°-grid (European Center for Medium-Range Weather Forecasts fifth-generation reanalysis for the global climate and weather; CDS, 2017). (b–e) Observed spectrograms between mid-January and mid-February 2016 for CDIP029, CDIP067, CDIP106, and CDIP166 (Behrens et al., 2019). The black dots indicate individual swell events identified by their long-period forerunner (Text S1).

either by utilizing the deep water dispersion relation in spectrograms observed at a point (Barber & Ursell, 1948; Hell et al., 2019; Munk, 1947; Snodgrass et al., 1966) or by estimating the local convergence of the wave ray's backward trajectories derived from SAR-images (Collard et al., 2009; Husson et al., 2012). Both methods assume swell systems to originate from an idealized source point. Clearly, the definition of such a source point may appear ambiguous, given typical spatial scales O(1000 km) and lifetime O (5 days) of an extra-tropical storm that moves at about 10 m s[1] (Figures 1a; Eady, 1949; Hodges et al., 2011; Neu et al., 2012).

A path to understand the appearance of such source points and the properties of the resulting swell systems, is to analyze the relationship between surface winds and the resulting surface wave spectra. This relation can generally be well approximated by a set of semi-empirical functions that assume homogeneous wind speeds within an area or for a certain duration: the fetch ("fetch laws," K. Hasselmann et al., 1973, 1976; Elfouhaily et al., 1997, and there in). However, these self-similar relations, first established by Kitaigorodskii (1962), do not account for the spatial and temporal variability of the wind forcing. It is thus unclear how a continuously varying wind field leads to the generation of one dominant single wave event that seems to stem from a very small source region, at least an order of magnitude smaller than the storm (Barber & Ursell, 1948; Collard et al., 2009; Hell et al., 2020; Husson et al., 2012; Munk, 1947).

Spectral wave models, like Wave Watch III (Tolman, 2009), have also known weaknesses due to their strong dependencies on the wind forcing field (Cavaleri, 1994; Durrant et al., 2013; Feng et al., 2006; P. A. Janssen

& Bidlot, 2018; Ponce & Ocampo-Torres, 1998; Stopa & Cheung, 2014). While parameterizations of the source terms in those numerical models essentially reproduce the fetch laws, modeled wave arrival times and heights are commonly biased compared to in-situ wave-buoy observations. These biases are likely related to some lack of precise information to describe storm dynamics. Extreme winds may not always be properly described over time and space, and generated swell systems cannot always be correctly predicted. This strong dependence of the modeled wave field on the wind forcing is also important when wave models are coupled to Earth system models to better represent surface fluxes and air-sea exchange (Bourassa et al., 2019; Li et al., 2016). In this case, wave model parameters cannot be tuned to compensate for biases in the wind forcing, and hence a better dynamical understanding of wave generation is still needed to include waves in coupled Earth system models.

An alternative to the fetch's scaling laws or spectral wave models is to consider simple wave evolution models, directly compared to wind and wave observations. Numerous studies have used this strategy for moving tropical cyclones (Bowyer & MacAfee, 2005; Chen et al., 2007; Kudryavtsev et al., 2015, 2021; Young, 1988, 2003; Young & Vinoth, 2013), but the relationship between faster moving extra-tropical storms and resulting swell events remains largely unexplored (Figure 1; Doyle, 1995, 2002; Young et al., 1987). Extra-tropical storms are an integral part of synoptic meteorology with ample theories about their dynamics and life cycles (Bjerknes, 1919; Neiman & Shapiro, 1993; Neiman et al., 1993; Schemm & Wernli, 2014, review in; Schultz et al., 1998, 2018; Shapiro & Keyser, 1990) and here we aim to connect these theories with dynamics of wave generation.

In this study, we explicitly show how synoptic-scale dynamics can be related to properties of the generated sea states and the residual swell systems. We build on developments presented in Kudryavtsev et al. (2015) to derive a simplified model for swell events from extra-tropical storms (Section 2.1). The goal is to complement full sophisticated spectral wave models, since a simplified model can rapidly provide large ensembles of solutions to help retrieve the storm properties. More explicitly, we approximate the moving fetch with varying winds under an extra-tropical cyclones as a two-dimensional Gaussian shape and analyze the dynamics resulting from gradients in the wind forcing field (Section 2.2). We then use a back-triangulating method to retrieve the swell source location from wave buoy observations (Sections 3.1 and 3.2). This allows us to test the idealized moving wind fetch model for several case studies in the North Pacific (Sections 3.3 and 3.4). Combining an idealized model for swell generation and the optimized model of swell propagation finally suggests a three stage life-cycle of swell waves that is, summarized and discussed in Section 4.

2. Wave Generation in a Moving Frame of Reference

In this section, we extend the framework introduced by Kudryavtsev et al. (2015) to extra-tropical storms. Wave spectra of growing seas are assumed to follow self-similarity, and dynamical changes of the spectra are described by a single variable, the peak angular frequency ω_p (K. Hasselmann et al., 1976; Kudryavtsev et al., 2015). The evolution of ω_p in an Eulerian frame is then described by

$$\frac{\partial \omega_p}{\partial t} + c_g \frac{\partial \omega_p}{\partial x} = \left(\frac{g}{u}\right)^2 \phi(\alpha), \tag{1}$$

where $c_g = \partial_k \omega_p = g/2 \, \omega_p$ is the peak group velocity, $\alpha = u/c_p = u\omega_p/g$ is the wave age, the ratio of the 10-m wind speed u and phase velocity of the spectral peak $c_p = g/\omega_p$ (Equation A8 in Kudryavtsev et al., 2015). The wind-input source term ϕ is defined as

$$\phi(\alpha) = \frac{q}{2}\left(\frac{c_\alpha}{\alpha}\right)^{1/q} \tag{2}$$

with $c_\alpha = 15.4$, and $q = -3/10$. Here, and in the following analysis, we use a set of parameters for a so-called young sea development (Badulin et al., 2007; K. Hasselmann et al., 1976; Kudryavtsev et al., 2015, details in Appendix A3). In the following, outlined dynamics remain the same for all possible choices of these parameters. Note that under constant winds Equation 1 is reduced to the familiar "fetch relations" (K. Hasselmann et al., 1973, 1976; Elfouhaily et al., 1997, and references therein).

The above equations solely describe the spectral peak variables (c_g, c_p and ω_p), but this is sufficient to derive the whole wave energy spectrum following semi-empirical relations (Elfouhaily et al., 1997; K. Hasselmann

et al., 1973; Pierson & Moskowitz, 1964). The total wave energy E and significant wave height H_s of the growing wave field are then related to the peak frequency ω_p with

$$\frac{E \, g^2}{u^4} = \frac{Hs^2 \, g^2}{16 \, u^4} = c_e \left(\frac{d \, g}{u^2} \right)^p \sim \frac{u \, g^2}{2 \, \omega_p^3}, \tag{3}$$

where $c_e = 4.41 \times 10^{-7}$ and $p = 1$, again following K. Hasselmann et al. (1976), Badulin et al. (2007), and Kudryavtsev et al. (2015). For this simple case of stationary wave generation, the energy of the generated wave field E travels with the group velocity c_g and hence can eventually leave the generation area. Over the open ocean, wave generation is related to patches of strong winds under storms, called the fetch, that are neither stationary nor infinite (Munk, 1947). The standard fetch relations are thus theoretical limits, and the fetch's characteristic scales and its propagation must be taken into account.

For a storm and its fetch that are both moving with the translational speed V, the wave-growth equation Equation 1 must be written in a Lagrangian frame of reference, moving with the storm as

$$\partial_t \omega_p + (c_g - V) \, \partial_X \omega_p = \left(\frac{g}{u} \right)^2 \phi(\alpha), \tag{4}$$

where $X = x - Vt$ is the along-wind coordinate in the moving reference frame (Kudryavtsev et al., 2015). This equation describes the evolution of a growing sea in the moving frame with coordinates (X, t), and the forcing $\phi(u, \omega_p)$ that is, a function of the local wind speed $u(X, t)$. This nonlinear first-order partial differential equation is used in the following two subsections to outline the effects of a moving fetch on growing waves for typical scales of extra-tropical storms. First for storms with constant winds for which the equation can be solved analytically (Section 2.1), and then with temporally and spatially varying winds following a Gaussian form (Section 2.2).

2.1. Constant, Finite Moving Wind Models

First, we consider constant steady winds u under a storm of length L and duration T, steadily moving with a constant translation velocity V. Constant winds imply a constant forcing function , such that Equation 4 can be solved analytically for ω_p using the method of characteristics (Appendix A). Figure 2 shows these characteristic curves of wave energy for typical scales of tropical and extra-tropical storms. The characteristic curves $X(t, X_0, t_0, c_0)$ describe the position of a growing nonlinear wave packet which has a group speed c_0 at position X_0 and time t_0, as it passes through the forcing field. Their first derivatives $\partial_t X \propto (c_g - V)$ describe wave energy's speed c_g relative to the speed of the moving frame V, and their curvature is proportional to the acceleration of this wave field and similarly the intensity of wave energy growth ($\partial_{tt} X \propto \dot{c}_g \propto \dot{E}$).

The initial sea is assumed to be at rest ($c_0 = 0$) such that the wave energy at the beginning of the storm ($X(t, X_0, 0, 0)$, Figure 2 bottom axis) is slow and propagates backward in the moving frame of the storm (for example in Figure 2a day 0–0.3). Even though these young seas propagate slower than the storm, their energy continues to grow because they are continuously exposed to the steady wind forcing. With time, the peak frequency decreases, and the group velocity of the peak wave energy increases (Equation 3). After a critical time τ_{crit} (dashed black line in Figure 2), the peak wave energy starts traveling at the same speed as the storm, that is, $c_g = V$. This timescale from the wind's onset until $c_g = V$ is

$$\tau_{crit} = \frac{c_\tau}{g} u^{-q} V^{1 + \frac{1}{q}}, \tag{5}$$

and the distance the storm has traveled during this time is

$$X_{crit} = \frac{c_\tau}{g} q u^2 \left(\frac{u}{V} \right)^{\frac{1}{q}}, \tag{6}$$

where $c_\tau(c_\alpha, q) = 1.23 \times 10^5$ and $q = -3/10$ measuring the efficiency of wave growth depending on the sea state (Appendix A).

While tropical and extra-tropical cyclones may have comparable translation velocities, tropical cyclones are smaller in scale, but can create very strong surface wind speeds for several days. This leads to a trapping or quasi-resonance of wave energy under tropical storms (Kudryavtsev et al., 2015). Trapping also appears
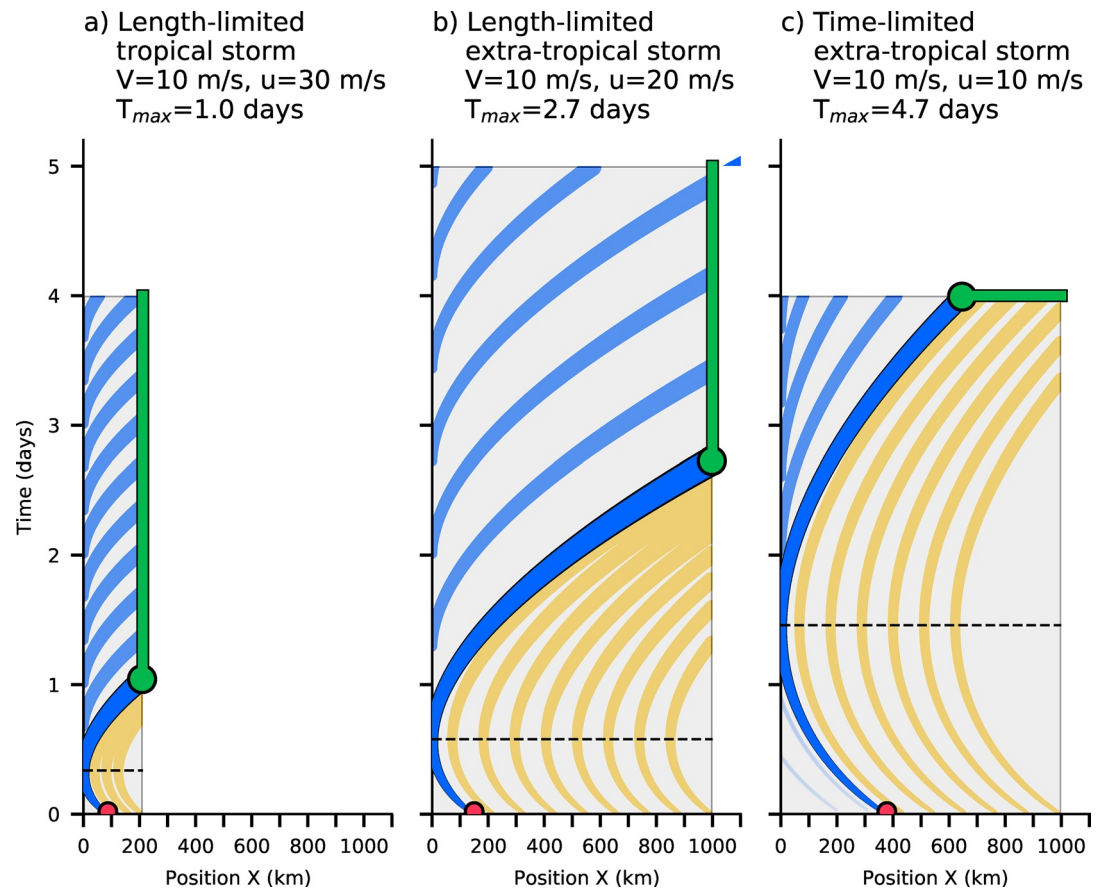
Figure 2. Characteristic wave energy curves for an idealized fetch model with constant and translating wind. (a) Characteristic curves for typical scales of a tropical cyclone ($V = 10$ m s^{-1}, $u = 30$ m s^{-1}, duration $T = 4$ days, length scale is 200 km, same parameters as in Kudryavtsev et al., 2015). The characteristic curves with lowest ω_p and the highest wave energy, that is, the longest characteristic curve (dark blue) start at the red dot (X_{crit}) and goes to its exit location (green dot). The green line indicates exit locations that have the same value of ω_p as the green dot, but in this case the wave energy was generated along the light blue lines starting after τ_{crit} (dashed black line). Orange lines indicate characteristic curves that start at t_0 but don't grow as long as the longest characteristic curve and result in smaller wave energy. The thickness of the characteristic curves is proportional to the wave's energy, or ω_p^{-1} (b) Same as (a) but for a length-limited extra-tropical storm with strong winds ($V = 10$ m s^{-1}, $u = 20$ m s^{-1}, duration $T = 5$ days, length scale is 1,000 km). (c) Same as (b) but for a time-limited extra-tropical storm with weak winds $u = 10$ m s^{-1}.

under extra-tropical storms that are large enough ($X > X_{crit}$, Figure 2 red dots), and, more importantly, last long enough ($t > \tau_{crit}$, Figure 2 dashed black line). Trapping can create more energetic (i.e., faster and longer) swell waves, because the growing sea-state remains longer under the forcing wind field than it would under a stationary wind field. Hence, only wave energy whose characteristic curves originate at a time larger than τ_{crit} or at a position larger than X_{crit} can end up propagating to the forefront of the moving fetch and being exposed to the maximum possible wind forcing (dark blue lines in Figure 2).

The trapping conditions are determined by the wind speed and translation velocity (Equations 5 and 6). Figure 2 illustrates how these critical scales differ between fetches of tropical cyclones (Figure 2a, $\tau_{crit} \approx 6$ to 10 h and $X_{crit} \approx 50$ to 100 km Kudryavtsev et al., 2015) and extra-tropical cyclones (Figures 2b and 2c, $\tau_{crit} \approx 12$ to 36 h and $X_{crit} \approx 100$ to 400 km).

The characteristic curves of wave energy under constant moving winds can then be separated into curves that leave the storm from the rear ($X_0 < X_{crit}$), curves that start further in the front ($X_0 > X_{crit}$) and reach the trapping condition, and finally curves that start at later time in the storm ($t_0 > \tau_{crit}$) and at the rear ($X_0 = 0$). For this last situation, the initial group velocity of the waves must be larger or equal to V, otherwise those
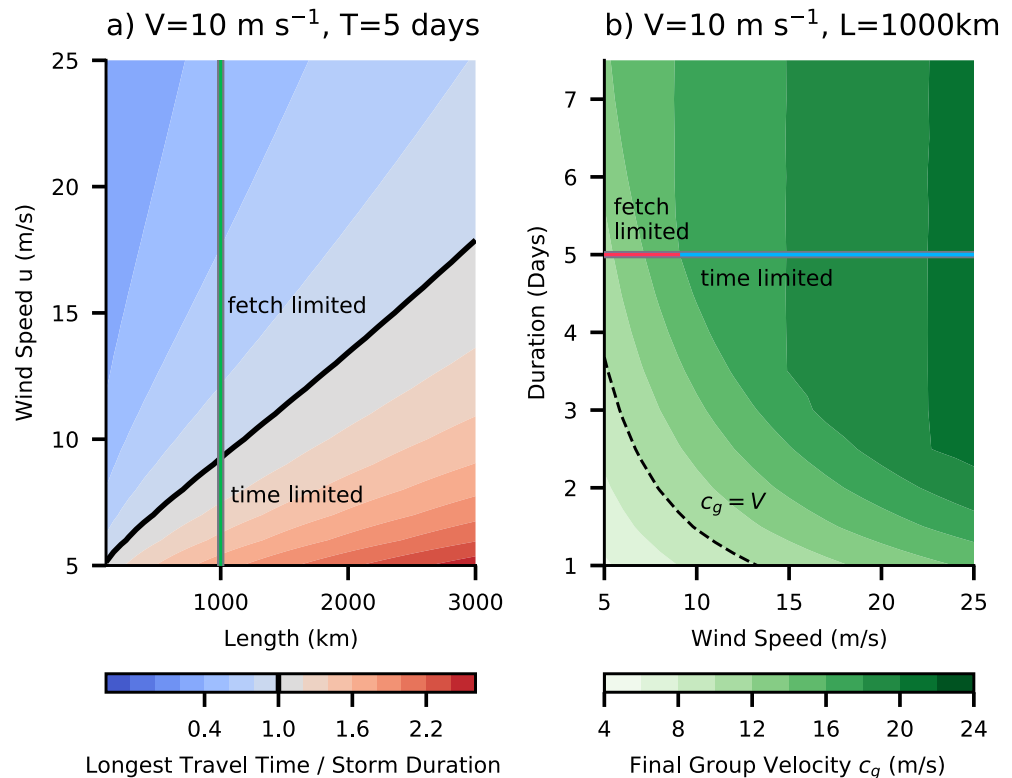
Figure 3. (a) Travel time of the longest characteristic divided by the fetch duration (5 days) for constant moving wind model with a propagation speed $V = 10$ m s^{-1} (as in Figures 2b and 2c). Blue shading indicates length-limited fetches, red shading indicates time-limited fetches and the black line shows cases with a travel time along the longest characteristic curve equal to the duration of the fetch. The green line indicates the parameter space in (b). (b) Group velocity of the longest characteristic curves of fetches with $L = 1,000$ km, translational speed of $V = 10$ m s^{-1}, but varying wind speed and duration. The trapping condition ($c_g = V$) is shown as black dashed line, while the fetch- and time-limited cases are shown as red and blue lines.

will not be able to propagate forward in the moving reference system and will leave the storm from the rear (Figure 2 light-blue curves, defined as $X(t, 0, t_0, V)$).

Characteristic curves for the three cases are separated by a special case corresponding to the longest, most energetic characteristic curve (Figure 2, dark blue line). It defines the largest generated wave energy for a given moving fetch and indicates if moving fetches are either "length-limited" or "time-limited." For length-limited conditions, the most energetic waves leave the storm before it terminates, and the swell properties are limited by the length scale of the storm (Figures 2a and 2b, green dot). For time-limited conditions, the maximum swell energy is limited by the duration of the storm (Figure 2c). For both cases, more than one characteristic curve is associated with the largest possible wave energy. Length-limited storms may last long enough such that more than one curve reaches the front of the storm. This implies a constant radiation of energetic waves from the front of the fetch, starting after a certain time from the onset of the storm (Figures 2a and 2b, green vertical lines). Time-limited cases may not last long enough for the curve starting at X_{crti} to reach the front of the storm. These cases result in most energetic waves leaving the storm in a spatial spread when it ends (Figure 2c, green horizontal line).

Extra-tropical storms can thus be either length- or time-limited (Figures 2b and 2c), while tropical storms mostly correspond to length-limited wave growth regimes (Figures 2a; Kudryavtsev et al., 2015). To illustrate this expected variability of extra-tropical storms, the effect of changes in the length, speed, and wind forcing on the largest generated group velocity along the longest characteristic curve is shown in Figure 3. For typical scales of extra-tropical storms (Figure 3a, green line), the fetches can be either time- or length-limited
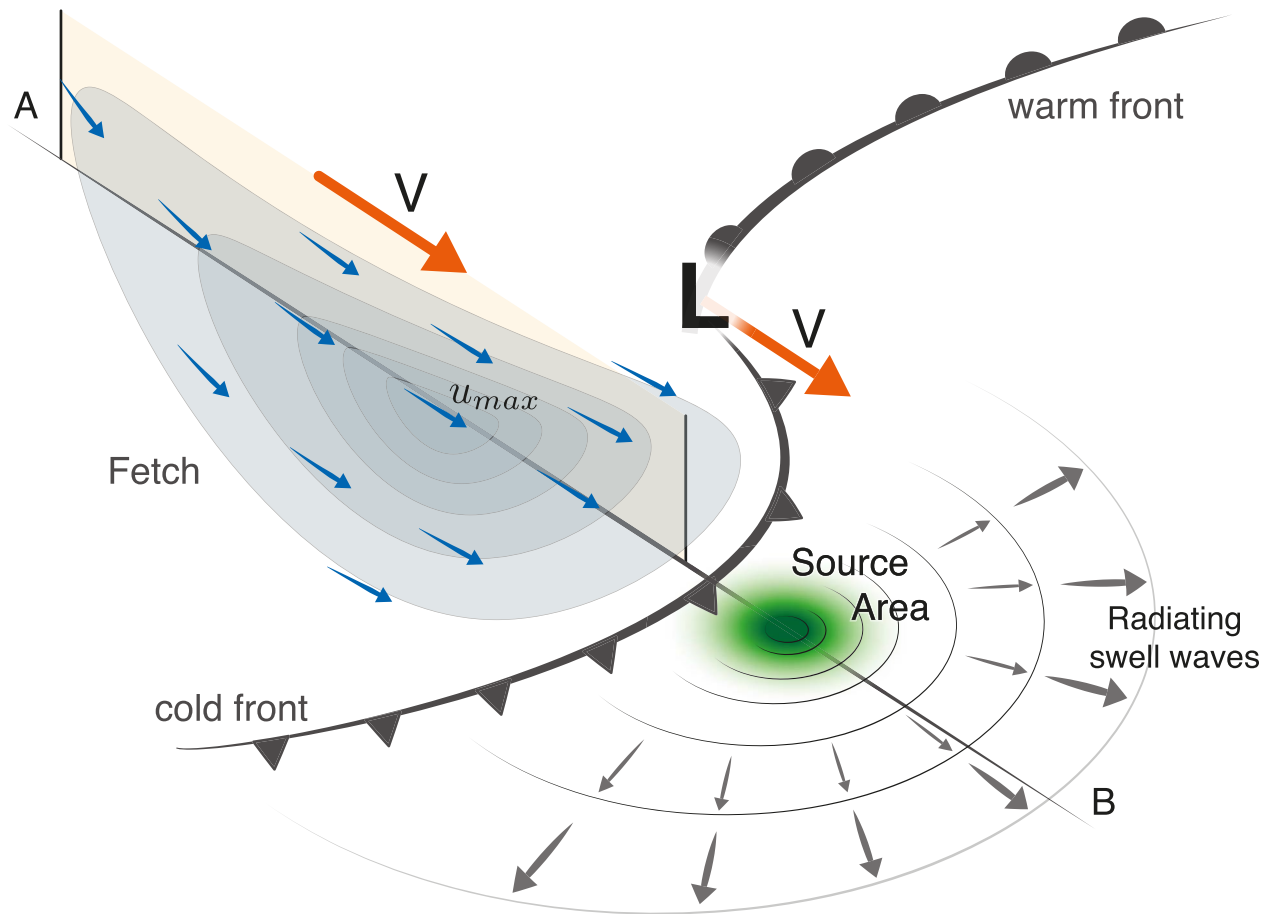
Figure 4. A moving fetch embedded in a Northern Hemisphere extra-tropical storm. The storms center L is adjacent by a warm and cold front (thick gray lines with half circles or triangles). The moving fetch is located behind the cold front (gray shading with blue arrows) and moves with the same translational velocity V as the cyclone center L (orange arrows) to the bottom right. The green area indicated the source region as suggested by a Gaussian moving wind model (Section 2.2) and observations (Section 3). Swell waves radiate away from this source region (small gray arrows).

(Figure 3a, black line). It is also possible that small extra-tropical storms do not even reach the trapping condition, as indicated to the left of the dashed black line in Figure 3b.

This constant-wind model outlines the general dynamics of swell generation under a moving storm and how its bulk spatio-temporal parameters affect the resulting swell systems. However, this conceptual model fails to explain why observed swell events have a clear temporal maximum (Figures 1b–1e) that seems to originate from a very small source location (Munk, 1947). In addition, this model implies that the forcing is constant within the fetch area and discontinuous at its boundaries.

2.2. A Gaussian Moving Wind Model

Hereafter, we relax the assumption of constant wind forcing to better represent the storm's life cycle and to account for the fact that observed winds vary smoothly over space and time. We now describe the wind forcing $u(X, t)$ in Equation 4 as a two-dimensional Gaussian function in space and time. This two-dimensional Gaussian moving fetch can be interpreted as representative of the wind patch typically established behind the cold front of a low-pressure system (Figure 4, gray shading) that travels with about the same translation velocity V as the storm (Figure 4, orange arrows). This fetch typically establishes on the equator-ward side of the storm and is tightly linked to the storm life-cycle (Neiman & Shapiro, 1993; Schemm & Wernli, 2014; Schultz et al., 2018), and could be called the "dangerous semi-circle," as under tropical cyclones (Arakawa, 1954; Sherman, 1956). Anticipating on the results of the observational analysis in Section 3, we assume
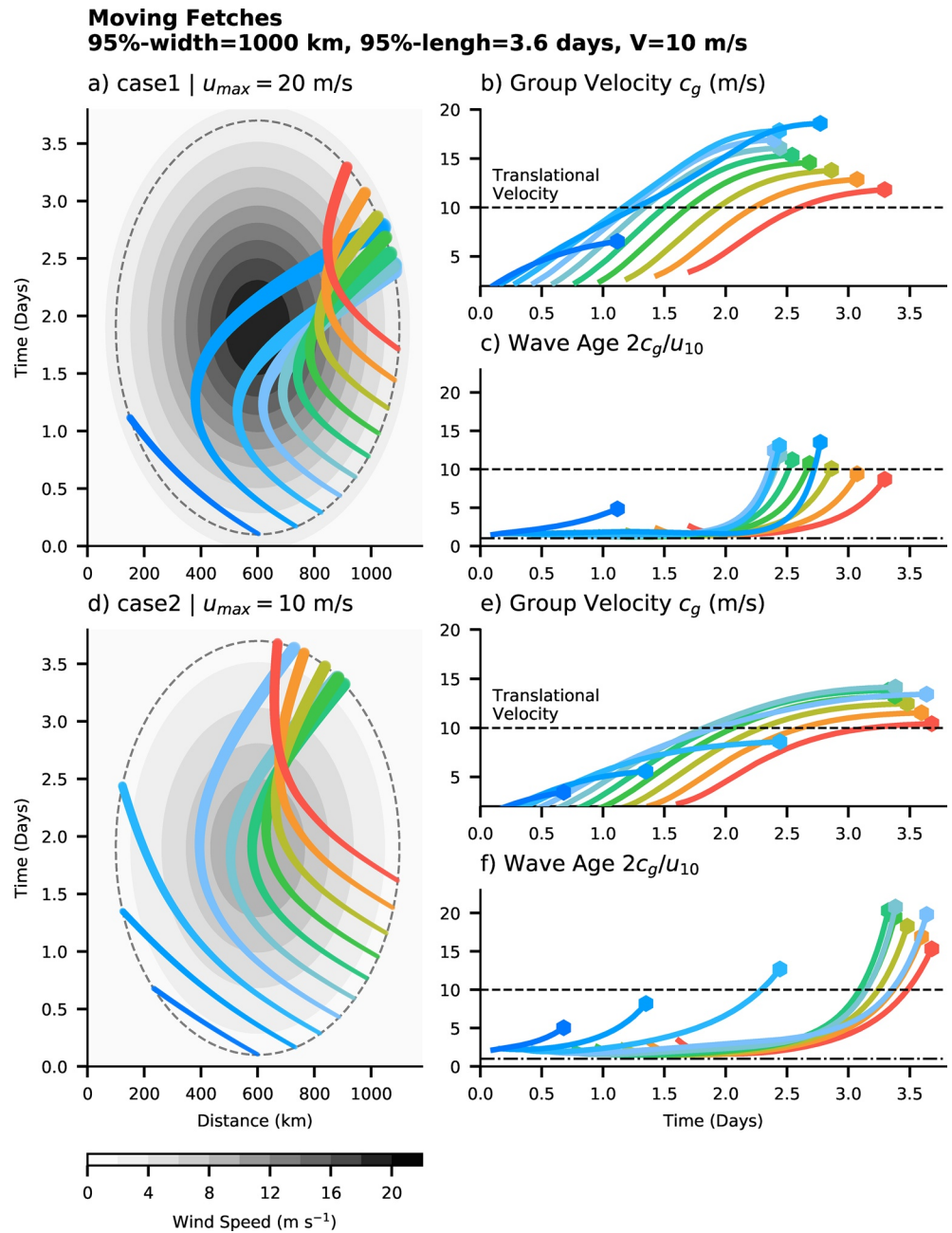
Figure 5. Characteristic curves from two-dimensional Gaussian winds in the moving frame of reference. (a) Two-dimensional Gaussian wind forcing (gray shading) with characteristic curves (colored lines) within the 95%-extension of the winds (black dashed lines). The wind forcing is defined by a 95%-width of 1,000 km, a 95%-duration of 3.6 days, a translational velocity V of 10 m s^{-1} and peak wind speed u_{max} of 20 m s^{-1}. (b) Group velocity along the characteristic curves as a function of time with colors same as in (a). The translational velocity $V = 10$ m s^{-1} is shown as black dashed line. (c) Same as in (b) but for wave age $\alpha = 2c_g/u_{10}$. The dashed-dotted and dashed line indicate $\alpha = 1$ or 10 respectively. Panels (d) to (f) as (a) to (c) but for peak wind speed $u_{max} = 10$ m s^{-1} rather then $u_{max} = 20$ m s^{-1}.

that the propagation direction of the fetch (Figure 4, orange arrows) is aligned with its dominant wind direction (Figure 4, blue arrows) and hence also aligned with the direction of the generated waves.

The space-time Gaussian wind forcing is defined by a wind speed maximum, u_{max}, a 95%-width, and a 95%-duration, while the 95% corresponds to ± 2 standard deviations of the Gaussian curve. Solutions of Equation 4 for two typical extra-tropical storms are shown in Figures 5a and 5d. A storm with a 95%-fetch-width

of 1,000 km, a 95%-duration of 3.6 days and $u_{max} = 10$ m s^{-1} shows characteristic curves similar to the length-limited case of constant winds (Figures 5a and 2b). The major difference is that characteristic curves converge and cross near the storm's leading edge, at the end of the storm's lifecycle (Figure 5a, day 2.5–3). The convergence of characteristic curves in a focus area results from the spatial gradients in the Gaussian wind forcing and does not appear with a constant, Heaviside-function wind forcing (Section 2.1). Hence, any realistic storm, with local wind maximum and smooth wind distribution, will have spatial gradients and focus characteristic curves from different parts of the moving storm.

The convergence of the characteristic curves show a focusing of wave energy by the superposition of wave trains and the formation of a convergence region (Figures 5a and 5d). The convergence and crossing of curves indicate that sea states with different generation histories (different paths of integration) propagate to the focal area and locally enhance the total wave energy spectrum. Enhanced wave energy will lead to increased dissipation and more nonlinear wave-wave interactions (S. Hasselmann & Hasselmann, 1985; Kudryavtsev et al., 2021), that is, the convergence of wave energy can add another forcing term in Equation 4. The largest estimated wave energies on the characteristic curves (Figure 5b, light blue to green curves) are thus likely lower-bound estimates, because independent solutions along the characteristics do not capture the expected enhanced dissipation and nonlinear wave-wave interactions due to wave energy convergence. Still, the proposed model is useful to explain the governing relations between the fetch scales and the moving storm, although it might lead to systematic biases for the total wave energies and peak wave frequencies.

The described wave-ray convergence leads to an area with significantly enhanced wave energy that can last for about half a day (Figure 5a between day 2–2.5 and Figure 5d between day 2.5 and 3). This area encloses the steepest waves of the wave generation process and is substantially smaller than the wind fetch that caused it (Figures 5a and 5d, gray shading). In the following, we argue that this small and distinct area acts as the source location for linearly propagating swell waves. From a distant location, it can be interpreted as a point source of swell waves (Section 3.2; Munk, 1947). This source location corresponds to the transition region from a nonlinear and very steep sea, mainly driven by wave-wave interactions, to a dominantly linear sea. In this transition region, the wind forcing decreases and subsequent wave-energy fluxes across frequencies vanish as well. The transition results in a linear sea that is, dispersive and its wave energy starts to travel as the superposition of linear waves. This interpretation of the characteristic curves focusing in a transition region predicts that an observable source location of swell systems should be displaced ahead of the strongest moving winds, rather than at the center of the high wind speed region. Observational evidence for this phenomenon is shown in Section 3.

2.3. Wave Age of Mature and Old Seas Under Moving Fetches

The Gaussian wind model emphasizes the nonlinear behavior of the wave energy growth and the importance of the wave field's generation history under the moving wind field. The wind forcing of sea states without a generation history can be solely described by the local wave age $\alpha = 2\,c_g/u$ (right hand side of Equation 4), because the nonlinear advection term is small and c_g is proportional to u (Figures 5c and 5f, day 0–2; Edson et al., 2013). However, once nonlinear advection increases, the wave energy growth cannot simply be described by the local wave age parameter (Figures 5c and 5f, day 2–3). These *mature* or *old seas* describe a situation where the simple relation between wave age, group velocity, and wind speed breaks down. While the group velocity only slowly grows, the wave age rapidly increases mainly due to constant or even decreasing local wind speeds.

A comparable wind forcing u on the right-hand side of Equation 4 can thus correspond to different degrees of wave development, that is, different c_g. When waves start to reach a mature state of development, the wind forcing starts to decrease and limit the peak frequency downshift. We expect this nonlinear behavior to be more important for *old seas*, that is, when the wave's peak phase velocity and the local wind velocity approach fully developed conditions of $\alpha \simeq 0.85$ (P. Janssen, 2004). In addition, wave energy convergence can counteract the local decay of the wind forcing and maintain a high wave steepness (see previous section). These focusing effects, associated with converging wave rays, should lead to enhancement and stabilization of the wave energy level. Thus, parametrizations of the wave's energy based on the local winds alone (e.g.,
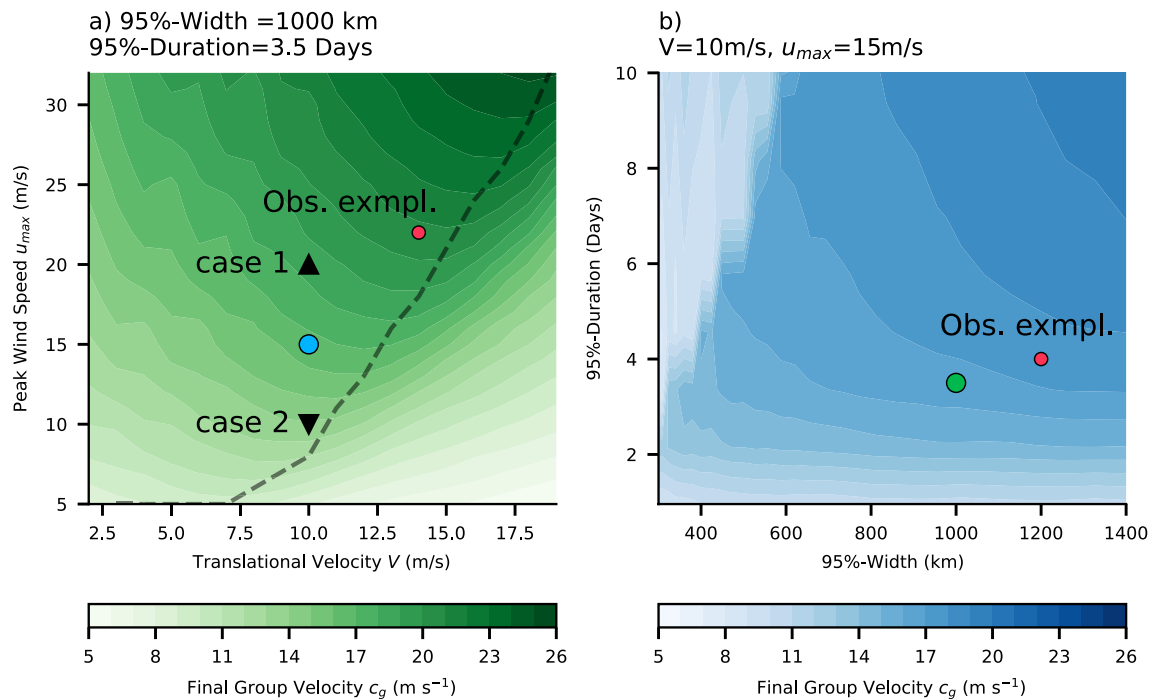
Figure 6. The dependences of the largest generated group velocity from the two-dimensional Gaussian wind model on the storm's scales. (a) Largest generated group velocities for varying translational velocity V and peak wind speed u_{max}. The dashed black line separates fetch- and time-limited cases. Cases 1 and 2 from Figure 5 are shown as the black upward- and downward pointing triangles. (b) Same as (a) but for changes in the 95%-width and 95%-duration. The parameter space of (a) and (b) are represented as green or blue dot in the respective other panel. The observational case from Section 3 (Figure 9c) is shown as red dot in (a) and (b).

Bourassa et al., 2013) may fall short under moving fetches of synoptic storms. A proper description of the wave energy needs to account for the nonlocal wave dynamics.

2.4. Scales of Extra-Tropical Storms Shape Wave Events

The spatio-temporal scales of extra-tropical storms thus govern the focal point of wave energy convergence and control resulting peak group velocities and wave energies. Using the Gaussian wind model, the spatial gradients are proportional to the ratio of u_{max} and the 95%-width. Since the average storms width is related to the Rossby radius and thus hard to change (Eady, 1949), the main control parameters become u_{max} and V. To illustrate this resulting sensitivity on u_{max}, Figure 5d shows a moving fetch with the same parameters as in Figure 5a, but for a weaker peak wind speed and hence a weaker spatial gradient. Compared to strong wind conditions, weaker winds temporally delay trapping condition $c_g = V$ and the location where the characteristic curves cross (Figure 5a, day 2–2.5 and Figure 5b, day 2.5–3) resulting in an overall lower group velocity.

A more systematic assessment is shown in Figure 6. Characteristic curves are calculated using Equation 4, but now for various combinations of storm sizes, duration, speeds, and wind forcing. For each set of storm conditions, we take the largest resulting group velocities to test the sensitivity of c_g on the storm scales. Because characteristic curves converge and cross, wave energies merge, and the largest c_g derived from the method of characteristics is likely to be underestimated (Section 2.2). However, this is still a useful metric to understand how the storm's scales control regimes of wave generation.

Comparisons between the peak velocity u_{max} and translation velocity V for typical scales of extra-tropical cyclones are shown in Figure 6a (95%-width and -duration are 1,000 km and 3.5 days). The two cases from Figure 5 are indicated by black triangles and illustrate how solely changes in the peak wind speed lead to different peak wave energies. Higher peak velocities u_{max} or faster-moving storms V lead to higher group velocities (Figure 6a, green shading). However, if a storm moves too fast, wave growth is limited because trapping effects are weaker or do not appear at all (Kudryavtsev et al., 2015, Figure 6a, to right of the black

dashed line). No trapping occurs for fast storms with relatively weak winds; a situation that is, likely uncommon for extra-tropical storms.

The fetch length and duration also affect the wave energy generation (Figure 6b). For typical but constant translation velocities and peak wind speeds, the wave energy increases when the storm is larger or lasts longer. However, more persistent storms are more effective in creating large wave energies than larger storms. For example, changing the storm size by 20% from 1,000 km to about 1,200 km has a weaker effect than changing the storm's duration by one day (Figure 6b, starting from the green dot). The importance of the storm's duration is again due to the trapping condition because trapping will always occur if the storm lasts long enough (Section 2.1).

3. A Case Study of a North Pacific Storm

In this section, we combine observed surface wave spectra with reanalysis surface winds to assess the consistency of the Gaussian moving fetch model for swell generation. We analyze the case of a single storm over the North Pacific and explain how dispersed swell arrivals in wave buoy observations provide strong evidence for a small swell source location. We employ a physically constrained machine learning methodology that heavily borrows from ideas in Munk (1947), Barber and Ursell (1948), Snodgrass et al. (1966), as detailed in Hell et al. (2019, 2020). This method triangulates the spatio-temporal coordinates of a single swell source which is simultaneously observed at five wave buoy stations. This helps to check wherever or not the hypothesis from Kudryavtsev et al. (2015) can be extended to extra-tropical storms with smooth Gaussian winds (Section 2; Figure 4), and if the swell source location is indeed displaced compared to the strongest observed wind forcing. We first give a brief overview of the algorithm used to establish the source location. A more detailed description of the algorithm and two additional case studies can be found in the Text S1 and Figures S4–S6. An example code is available at https://doi.org/10.5281/zenodo.5201953.

3.1. Physically Constrained Optimization of a Parametric Swell Model—In Brief

We designed a parametric swell propagation model that is, optimized on five pre-identified wave events. The spectral shape of the parametric model is described by a commonly used shape function (K. Hasselmann et al., 1973; Elfouhaily et al., 1997), it's time component as an Erlang distribution (Hell et al., 2019), and its decay as a function of the travel distance (Jiang et al., 2016, Text S1.3).

The optimization is performed in five steps. First, swell wave events observed by the Coastal Data Information Program (CDIP) wave buoy network (Behrens et al., 2019) are identified in the very long swell band. Second, the parametric model is fitted to each swell event at each wave buoy observation, and the uncertainty of its parameters are estimated to evaluate the spectral dispersion slope and the quality of the observation (Hell et al., 2019). Third, the swell events are matched by their estimated initial time that can be inferred from the events dispersion slope (Barber & Ursell, 1948; Collard et al., 2009; Munk, 1947; Snodgrass et al., 1966). In the fourth step, these sets of matched swell events are used to compare with parametric model outputs, but now assuming a common isentropic point source origin. Given a resulting hypothetical source point, the parametric model provides dispersion slopes, arrival times, and the wave's amplitude attenuation for each member in the set of swell observations. A combined cost function is then optimized for the common source point as described in the following (Section 3.2).

The algorithm's robustness largely builds from the fact that swell observations carry information about their source location. The radial distance to a source location is indirectly measured by the dispersion slopes of the wave events spectrograms (Barber & Ursell, 1948; Collard et al., 2009; Munk, 1947; Snodgrass et al., 1966). The combination of three or more buoy observations generally provides sufficient means to retrieve a common source location of the swell. Here, we use observations at five locations to reduce errors due to the spherical geometry and potential distorted observations at one or more location (see next section). Details about this algorithm, the parametric swell model and the cost-function design are given in the Text S1.
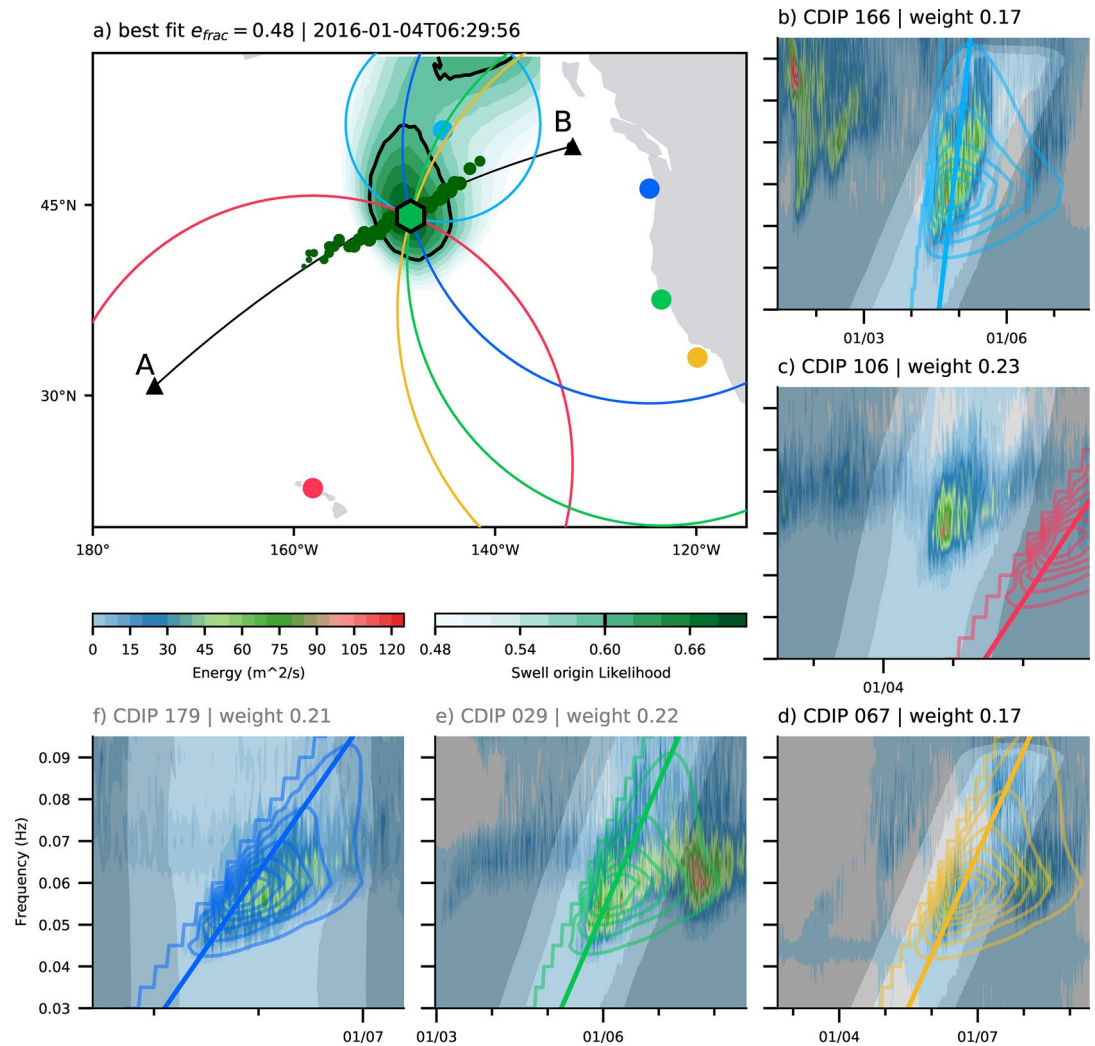
Figure 7. Results for the source point optimization for the case study in January 2016. (a) The colored circles show the best fit great-circle distanced for the respective stations (colored dots). The great-circle radii correspond to the sloped lines in panel (b) to (f) and the green hexagon is the position of the most likely common origin on January 4, 2016 at 06:00 UTC. The green shading shows the likelihood measure $L_{e_f} > 0.5$ for this time step and the black contour the corresponding likelihood of $L_{e_f} = 0.6$. (b–f) The fitted parametric models (contours) compared to the station data (colored shading). The gray shadings in panel (b) to (f) is the weighting on the data during the optimization, and the weight in the sub-titles is the data's weight in the multi-station cost function (Text S1).

3.2. Triangulation of Swell Origins

The cost function between the parametric model and the data helps to quantify the performance of the model fit. A map in longitude, latitude and time of most likely wave origins is derived to define a measure on the model fit. A likelihood $L_{e_f} = 1$ indicates a perfect model fit and implies that all data variance is explained by the model, while $L_{e_f} = 0$ indicates total model failure (Equation 11 in Text S1.5).

The result of the optimization is shown Figure 7 for a storm between the January 4th and 8th, 2016 (Figures S4 and S6 for other examples). The green hexagon in Figure 7a indicates the most likely common source location for the swell events detected at five buoys (Figures 7b–7f). The identified source location on January 4, 2016 at 6:30 is identical for either a brute-force search in the parameter space, or a global cost minimization (within a 25-km radius and 1 h, Figure S1).

Even though both methods return a source location close to ocean station PAPA (CDIP 166), they somehow lead to different interpretations of the process of swell generation. While the global optimization returns a single optimum that would indicate a common point source for the wave's energy (Munk, 1947), the brute force method is in principle less precise but can hint at multiple areas of similar likelihood. It samples a broader parameter space and hence can provide a likelihood map of swell origins (Figure 7a, green shading).

Note that the assumption of a single optimum essentially follows the idea of a linear inversion of the observed dispersion slopes in observations (Figures 1b–1e and 7b–7f; Munk, 1947), which in turn directly implies the existence of a point source (Figure 7a, green hexagon). However, the brute force method optimizes a cost function designed under the assumption of this point source, but it returns a multitude of location with similar likelihood (Figure 7a, green shading). The assumption of an idealized point source is still a reasonable interpretation for a single distant observer of swell, but some refinement is needed in the context of the transient wave generation and decay (Section 3.4).

The brute force sampling shows how the maximum of L_{e_f} shifts in space for a sequence of time steps (Figure 7a, green dots). It means that observed waves either originate earlier from a position west of the most likely source location, or later from a position east of the most likely source location (Figure 7a, green dots). This trace of local maxima in L_{e_f} can be interpreted as a progression of wave origins rather than a single point, as suggested by the constant or Gaussian wind models (Figures 2b, 2c and 5). This trace of local maxima in L_{e_f} is used in the next section to combine the observed wave events with observed wind patterns that are related to propagating storms.

Note that a successful optimization of the multi-station cost function may not always be straightforward. Indeed, local wind swell and wave-current interactions on the swell travel paths are able to distort the wave buoys observations (Gallet & Young, 2014; Villas Bôas et al., 2017), and possibly alter the optimization procedure (Hell et al., 2020). Figures 7b–7f compares instances of the parametric wave model (colored contours) for the most likely source location (green hexagon in panel a) to the respective observations (colored shading). The parametric model captures the observed dispersion slopes in four out of five cases. Comparison between the model and data from CDIP 106, close to Hawaii (Figure 7e and red dot in Figure 7a), indicates a modeled wave arrival about 1 day later and further away than the observation. Hence, the observed wave event close to Hawaii could result from a closer source than suggested by the best model fit, and still be related to the same storm system. In such a case, a different growth history, that is, a different effective fetch, would be necessary. This case study shows that a more holistic understanding of the optimization hints at the complexity of wave generation in the real world, but also shows that even imperfect and distorted data can support the hypothesis in Section 2.2.

3.3. Comparing Observed Swell Origins to Reanalysis Winds

To interpret the relation between possible wave origins and the wind pattern that creates them, we show three snapshots of surface winds and sea level pressure from hourly ERA5 reanalysis on a 0.25°-grid in the North East Pacific (Figure 8, European Center for Medium-Range Weather Forecasts fifth-generation reanalysis for the global climate and weather; CDS, 2017). The storm propagates eastward, and its associated strong surface winds, the fetch, move eastward as well (red area at about 160°W and 40°N in Figure 8a moves to about 150°W and 50°N in Figure 8c). The same propagation can be seen for the local maxima of L_{e_f} and hence for the source location of swell (Figure 7a, green dots). Interestingly, the swell origins appear systematically ahead of the highest wind speeds (Figures 8a–8c). This displacement between the swell origins, estimated from wave buoys, and the highest wind forcing, estimated from reanalysis, is the same as predicted for swell generation by a moving fetch (Section 2.2). Hence the physically informed brute-force optimization shows how the trace of most likely swell origins, that is, a trace in the local maximum of L_{e_f}, co-travels with the patch of highest wind speeds under a moving storm.
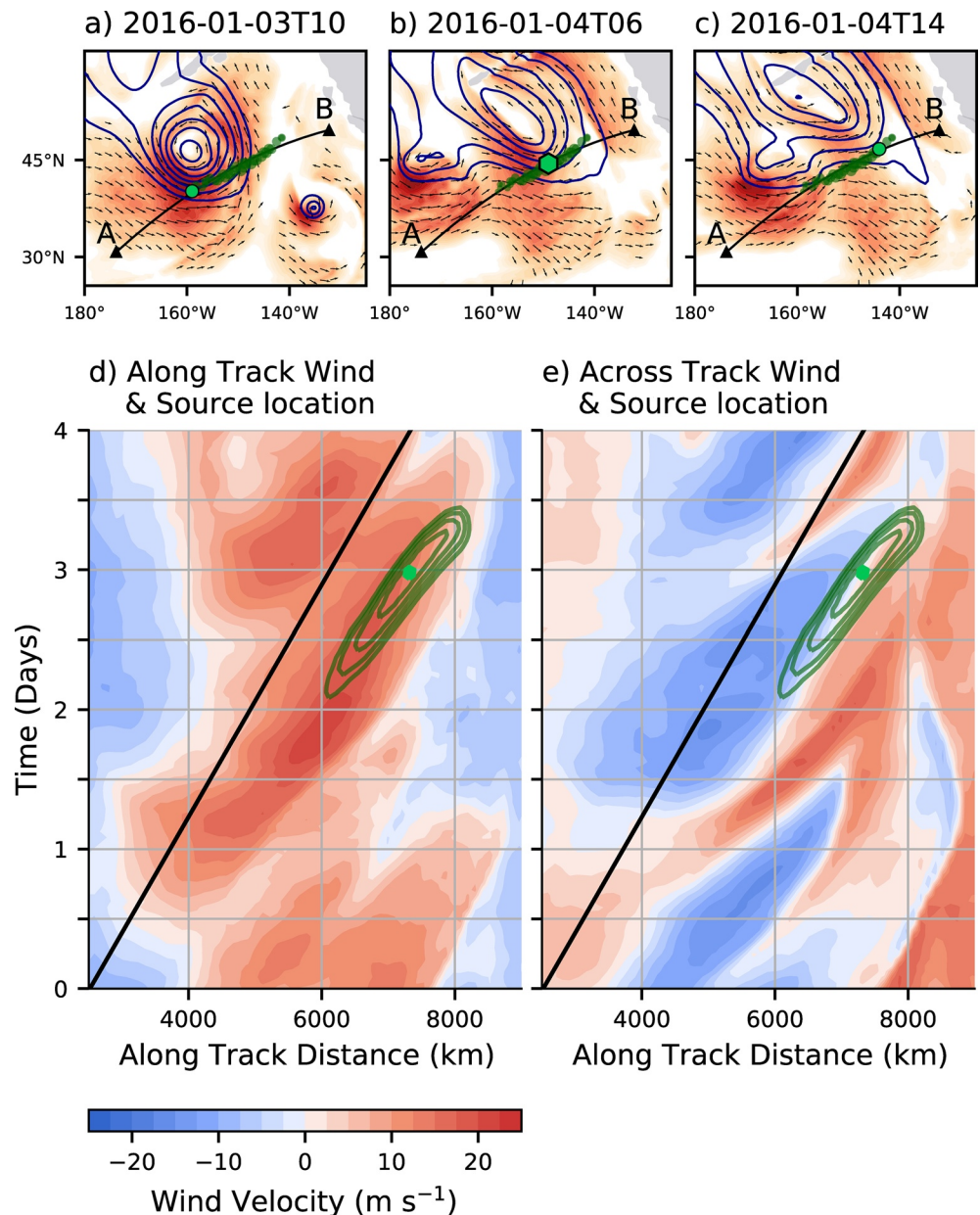
Figure 8. Optimized source locations compared to reanalysis winds (shading and vectors as in Figure 1) and negative SLP anomaly (dark blue contours as in Figure 1) for a date early in the event (a, 2016-01-03 10:00), the most likely origin time (b, 2016-01-04 04:00), and late in the event (c, 2016-01-04 14:00). The light green dots or the hexagon represent the most likely swell wave origin for the respective time step and the dark green dots are most likely swell wave origins for all time steps. The black line between the point A and B is a least-square fit to these dots of most likely origin and defines the transect through the wind data in panels (d) and (e). The transect through the wind data between point A and B is shown for along-transect (d) and across transect (e) winds. The wind data are indicated in red and blue shading, the area observed of most likely wave origin as green contours ($L_{e_f} \geq 0.6$), and its maximum as green hexagon. The estimated translational velocity along the transect is shown as black line (see Figure S2).

3.4. Computing Waves Growth From Realistic Moving Winds

We can now compare the propagating, co-located winds patches and swell origins to the moving Gaussian wind model. To do so, we transform the surface winds in a Lagrangian frame using its average propagation speed.
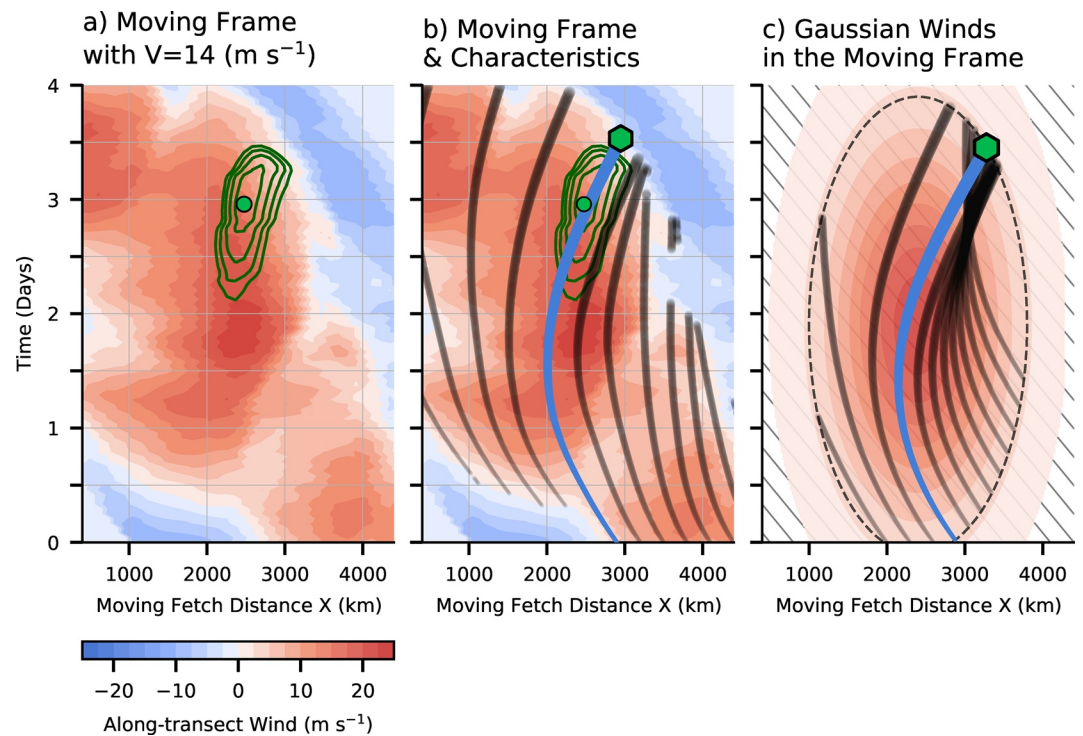
Figure 9. Observed winds in the moving frame of reference. (a) Same as Figure 8d but in the moving frame of reference. The black line Figure 8d would be here a vertical line. (b) Same as (a) but with characteristic curves of ω_p solving Equation 4 with the method of characteristics. (c) Same as Figure 5a but for scale estimated from (b): 95%-width = 2,800 km, 95%-duration = 4 days, $u_{max} = 22$ m s^{-1}, and $V = 14.1$ m s^{-1}. The characteristic curves with the highest wave energy are marked as blue line in panel b and c and the green hexagon indicates the position where wave growth can terminate the latest. The dashed black line in (c) is the 95%-boundary of the forcing field.

We first define a transect line for the wind data using a least-square fit to the trace of L_{e_f} (Figures 8a–8c, straight black lines between A and B). Next, we take data along this transect over a width of 440 km from the wind reanalysis between the points A and B. The wind is rotated to along- and across-transect velocities and then averaged orthogonal to the transect (Figure S2). The resulting time evolution of the along- and across-track averaged winds as well as contours of L_{e_f} are shown in Figures 8d and 8e. Finally, we estimate the average propagation speed V of the along-transect wind patch using again a least square fit (Figures 8d and 8e, black sloped line, Figure S3). The estimated propagation speed V of 14.1 m s^{-1} is then used to shift the data in the frame of reference of the moving wind patch.

The resulting along-transect velocities and the contours of L_{e_f} are shown in the moving frame of reference in Figure 9a. The area of most likely swell origin is clearly displaced in space and time compared to the highest wind speeds (Figure 9a, green contours and red shading). The most likely swell origin is about one day delayed compared to the strongest winds. It is thus unlikely that the observed swell waves originate from the area of highest wind speeds. Instead, swell waves are delayed in the moving frame of reference. A temporal delay in the moving frame implies also a spatial displacement in the Eulerian frame, as already observed in Figure 8. This space-time displacement cannot be explained by the stationary fetch laws, which only describe swell properties away from a constant-wind "fetch" area (Section 2; Elfouhaily et al., 1997; K. Hasselmann et al., 1973; Kitaigorodskii, 1962). This space-time displacement is in line with the predicted delay in the moving frame of reference between strongest wave growth and linear swell propagation dispersion (Section 2.2).

The spatial-temporal delay of the estimated wave origins can be explained by analyzing the characteristic curves of wave growth forced with the transformed wind data. As in Section 2.2, we use the method of characteristics to solve Equation 4 but now using the along-transect reanalysis winds in the moving frame of reference (Figures 9a and 9b, shading). The characteristic curves are initialized from a sea at rest ($\omega_p \approx 20\pi$ s^{-1},

Appendix A) where the winds are zero ($u = 0$) and represent paths of wave energy growth that propagate in the moving reference frame (Figure 9b, black and blue contours). As in the idealized model (Section 2.2), the line thickness shows that wave energy and group velocity increase along the path while ω_p decreases. Several characteristic curves reach the trapping condition ($V = c_g$) and some paths converge and cross due to large-scale gradients in the wind forcing (Figure 9b, day 2.5–3.5, see also Figure S5 for another case study).

The path with the largest final wave energy is shown in blue in Figure 9b. This characteristic curve is terminated, where the wind forcing reaches zero (Figure 9b, green hexagon), indicating the last space-time location of possible active wave growth. While this is a practical definition of where wave growth decays, because Equation 4 only captures wave growth, it is remarkable that the longest characteristic curve overlaps with the area of most likely swell origin and crosses its peak (Figure 9b, green dot and contours). Even though this area of most likely origins is transformed in the moving frame of reference, it is derived independently from the solutions of the characteristic curves. And, while the wind forcing of the characteristic curves is taken along the trace of the triangulated swell origins (Section 3.2), there is no need for the longest characteristic curve to match the independent buoy observation. This match between the forward calculation of the wave growth model forced by reanalysis winds (Equation 4) and the back triangulation of linear swell propagation (Figure 7) provides evidence that the conceptual idea of a Gaussian wind model (Section 2.2) is sufficient to capture the necessary dynamics of wave growth and swell generation by a moving storm. This is, to some extent, surprising given the nonlinear nature of Equation 4 and potential biases in the surface winds (Allen et al., 2020; Gille, 2005; Hell et al., 2020; Ribal & Young, 2019; Trindade et al., 2020; Wentz et al., 2015).

To further explain why wave growth from transformed reanalysis winds is able to match the triangulated swell origins, we use the Gaussian wind model from Section 2.2, for parameters that match the scales of the observed wind forcing ($V = 14.1\,\mathrm{m\,s^{-1}}$, $u_{max} = 22\,\mathrm{m\,s^{-1}}$, a 95%-duration of 4 days and 95%-width of 2,800 km, Figure 9c). The Gaussian wind model is able to reproduce and predict a trajectory of the largest wave energy align with the observed source locations (compare Figures 9b and 9c, blue line and green dot). It captures the observed larger-scale spatial and temporal wind gradients that are needed to create the convergence of the characteristic curves (Figures 9b and 9c). This provides evidence that a Gaussian moving fetch is a sufficient model to understand swell generation by extra-tropical cyclones (see Figures S4–S6 for additional examples).

4. Discussion and Conclusion

Swell wave generation from extra-tropical storms is a long-standing problem (Munk, 1947). Here, we presented a comprehensive explanation of why swell systems likely originate from small locations that do not necessarily match the high wind forcing regions. This explanation points to aspects in the process of swell generation that need to be better captured to improve wave forecast models but are also relevant for estimating air-sea fluxes and ocean mixed-layer variability.

A two-dimensional Gaussian wind model is found to be sufficient to represent the wave generation under a moving storm and to improve upon constant wind forcing conditions (Sections 2.1 and 2.2). The storm and its cold sector are assumed to travel with a constant translation velocity (Figure 4), even though in reality, the storm's fetch propagation might likely vary in speed and direction. The proposed model is highly idealized but is still detailed enough to capture the main wave-generation mechanism during the life-cycle of an extra-tropical storm as for example, described in Neiman and Shapiro (1993), Neiman et al. (1993), Schemm and Wernli (2014), and Schultz et al. (2018). It is also found to be a sufficient minimal model to explain observed displacements of estimated swell source location compared to the highest wind forcing locations (Section 3.3; Figures 9b and 9c; Hell et al., 2020). The combination of a Lagrangian wave-growth model with an optimized swell propagation model suggests three stages in the life cycle of swell wave energy.

- **Stage 1: Wave Growth Under a Moving Fetch in a Young and Growing Sea**
  Starting from a sea at rest, wind forcing creates short waves as a result of wave-wave interactions, wave growth and dissipation. Wave-wave interactions lead to a continuous decrease of the peak frequency ω_p, while the total wave's energy and significant wave height increase (Equation 3). For an actively growing
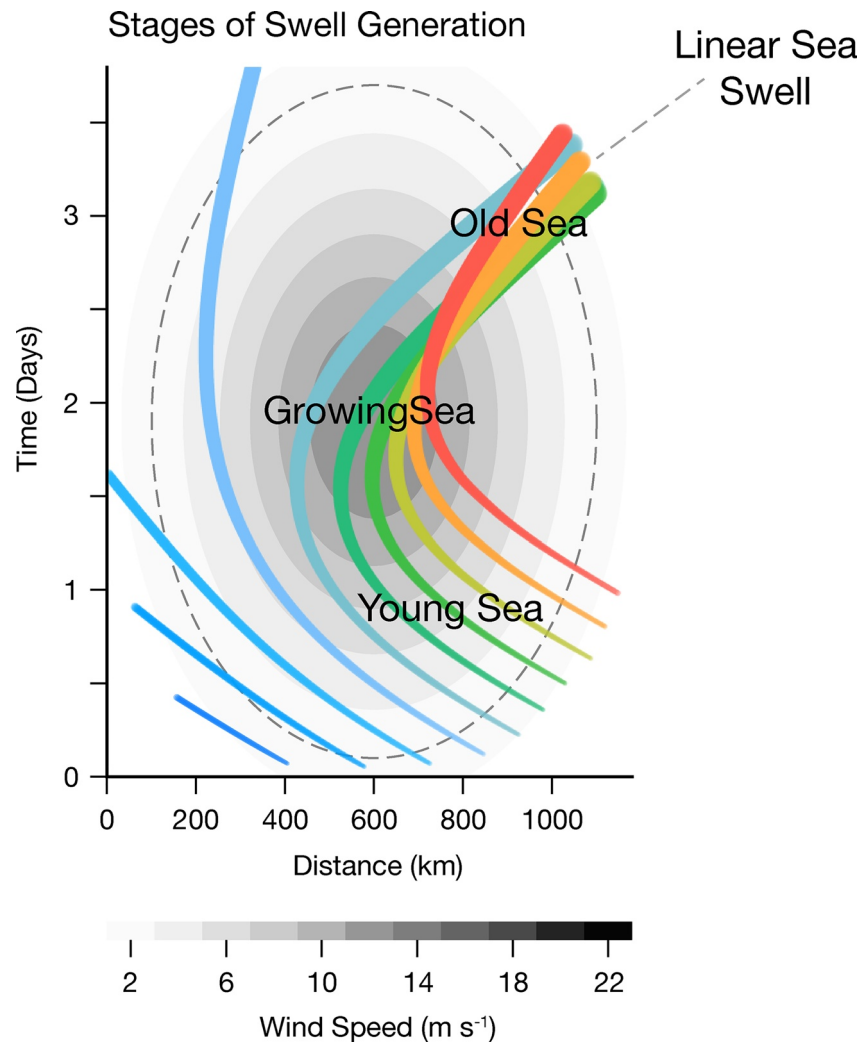
Figure 10. Schematic of wave growth under a moving storm with Gaussian wind. The gray shading shows the wind forcing and the dashed gray line marks the 95%-boundary of the Gaussian wind forcing. The colored lines are characteristic curves of wave generation in the reference system of moving extra-tropical storm. Wave growth starts with a *young sea* from rest and a small peak group speed. It develops into a *growing sea* that travels at the speed of the storm, until the wind forcing retires in an *old sea* such that the sea state eventually stops growing and the nonlinear wave-growth terms decay. Once the wave energy in each frequency band is dominantly linear the wave energy disperses and travel as *linear sea*, that is, swell.

wave field, the wave energies in different frequency bands are strongly coupled through wave-wave interactions. This coupling likely inhibits frequency dispersion and let us uniquely describe the wave spectra by its peak parameters. The energy of the nonlinear sea state thus mainly travels with the group velocity of its dominant frequency $c_g(\omega_p)$ shown by characteristic curves in Figure 10.

At first, waves are slower than the storm and propagate backwards in the moving frame of reference. With time this *young sea* continues to grow, its peak frequency decreases, and the associated group velocity accelerates (Figure 10). Eventually, the wave's energy starts to propagate with a speed comparable to the storm, such that the wave energy is trapped under the storm ($c_g = V$, Section 2.1). The wave's energy is now strongly growing because the previously established nonlinear sea is exposed to the strongest winds of the moving fetch (*growing sea* in the center of Figure 10). This process ends when the wave energy leaves the storm or when the wind forcing vanishes.

This strong wave energy growth depends on if the wave's energy is trapped ($c_g = V$) or not. This trapping, or quasi resonance (Bowyer & MacAfee, 2005; Dysthe & Harbitz, 1987; Kudryavtsev et al., 2015;

Young, 1988; Young & Vinoth, 2013), mainly depends on the ratio of the wind speed to the translation velocity (Equations 5 and 6). Wave energy is more easily trapped if the translation velocity of the storm is small or the wind speed is high (Figures 3b and 6a).

- **Stage 2: Decay of Nonlinear Terms in an Old Sea**
  When the wind forcing decays, the wave energy does not immediately turn into linearly propagating swell. Instead, dissipation may remain active, with the wave-wave interactions countering the wind forcing decay. The peak frequency downshift ceases and the waves's steepness starts to decrease. Hence, the still steep nonlinear sea decays (Kudryavtsev et al., 2021). This results in a transformation to progressively more linear sea (*old sea*, Figure 10). Timescales on which the nonlinear terms in the wave-action equation decay are inversely proportional to the fourth power of the wave steepness and are typically about three hours (Zakharov & Badulin, 2011; Zakharov et al., 2019). During this time, the wave field transforms from a nonlinear (steep wave spectrum) to a dominantly linear sea state (broader wave spectrum). Because the wave field still propagates during this relaxation time, the location where the wave spectrum is dominantly linear differs from the last location where the wind was still substantially growing waves.

- **Stage 3: Linear Propagation of Swell**
  Once the wave field becomes linear, the wave energy in each frequency band propagates following the deep water wave dispersion relation as a *linear sea* (Figure 10 and radial propagation in Figure 4). At this stage, almost no interaction occurs between the different frequency bands. From this point on, the travel distance and energy attenuation are proportional to the amount of dispersion, which in turn is the difference in the arrival time between waves of different frequencies (Text S1.4; Ardhuin et al., 2009; Barber & Ursell, 1948; Munk, 1947). A backward triangulation based on linear propagation as in Section 3 can then be applied successfully, as long as the swell's interactions with currents, eddies, and other wind forcing remain weak along its great circle path.

The Gaussian wind model is a smooth forcing field that can also be related to the scales of extra-tropical storms (Figures 6 and 11). Four parameters characterize the moving fetch; its translation velocity V, its length-scale along the peak wind direction (95%-width), its lifetime (95%-duration), and its peak wind speed u_{max}. All of them are determined by synoptic-scale dynamics. It follows that processes that influence the storm's intensity may also influence the shape, amplitude, and peak period of the observed swell events (Figure 11). This analysis provides a practical means to connect observed swell events to storm characteristics and confirms that nonlocal swell measurements can be used to quantify storms over the open ocean (Hell et al., 2020). This can further link the current and future swell wave climate to common diagnostics of extra-tropical storms (Figure 11; Hoskins et al., 1985; Schemm & Wernli, 2014; Schultz et al., 2018) and their statistics (Andrews & McIntyre, 1976; Bengtsson et al., 2006; Charney, 1947; Eady, 1949; Mbengue & Schneider, 2016; Shaw et al., 2016, and others).

The idealized model of a moving fetch suggests that wave event intensities are most sensitive to spatial gradients in the wind forcing fields (Figure 6a). Since the average size of storms, and their fetch (1,000 km), are constrained by basic properties of Earth's mid-latitudes flow (Bengtsson et al., 2009; Catto, 2018; Eady, 1949; Hodges et al., 2011; Sinclair et al., 2020), the spatial wind gradient is mainly determined by the peak wind speed u_{max}. A larger peak wind speed and a stronger spatial wind gradient lead to more efficient trapping of the wave energy, with the consequence of larger swell waves. Note that at the leading edge of the moving fetch, the spatial wind gradient is related to the complex dynamics at the storm's cold front. The Gaussian wind model (Section 2.2) is a sufficient minimal model to explain the underlying dynamics but may not fully capture these smaller-scale wind gradients. It can be easily extended by introducing non-Gaussian corrections to the spatial wind distribution.

Intensities of wave events are also sensitive to the ratio of the peak wind speed u_{max} and storm propagation speed V because they are key to determine the trapping conditions (Equation 6). If their ratio, u_{max}/V, is relatively large, the trapped wave energy leaves the wind forcing at its leading edge, co-located with the storm's cold front (Figures 4 and 7e). This can be interpreted as a "length-limited" fetch (Figures 2b and 5a). In contrast, if u_{max}/V is small the trapping is less intense and the wind forcing may decay before the wave energy reaches the leading edge of the fetch. This is better interpreted as a "time-limited" fetch (Figures 2c and 5d).
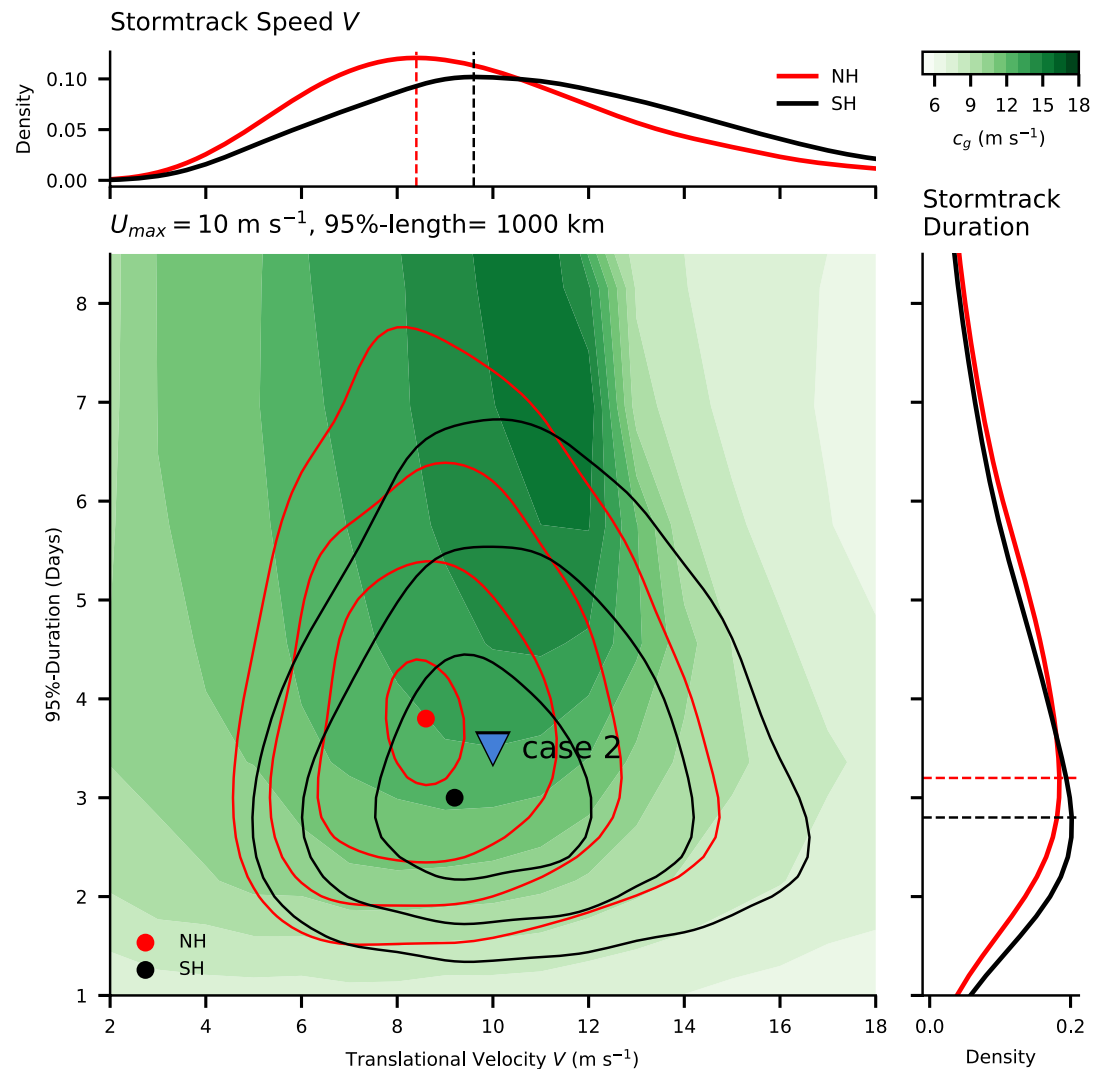
Figure 11. Peak group velocity c_g of wave events from a Gaussian wind forcing of different velocity V and duration. The given peak wind speed and 95%-width are predefined as $u_{max} = 10\ \mathrm{m\ s^{-1}}$ and 1,000 km. The joint distributions of storm track speeds and lifetime are shown for the Northern Hemisphere (red) and Southern Hemisphere (black) as contours and their maxima as colored dots. The results for scales of a Gaussian wind forcing as in Figures 5d–5f are shown as blue triangle. The storm track statistics are derived from reanalysis sea level pressure fields using Murray and Simmonds (1991a, 1991b). Note that this algorithm does not provide a peak wind speed u_{max} such that we assume 10 m s^{-1}, even though we point out that u_{max} is an important parameter for the resulting peak group velocity.

Length- or time-limited fetches may frequently occur under extra-tropical storms (Figures 3, 6 and 11), while tropical storms usually reach a length-limited situation that constantly radiates waves (Figure 2a). Under such a condition, the generated wave field would depend only on the storm's propagation velocity (Kudryavtsev et al., 2015).

Reanalysis products have biases in their representation of wind extremes (Gille, 2005; Hell et al., 2021). These wind extremes are represented in the Gaussian model as the peak wind speed. The sensitivity of the resulting swell peak period to the peak wind speed (Section 2.4) indicates that biases in wind extremes can cause biases in wave models by altering the processes of wave growth (Aouf et al., 2021). Errors in the peak wind speed of a few meters per second change the spatial wind gradients, alter the location of the highest energy convergence, and consequently the location where the swell energy starts to travel as linear waves. This might result in biases in arrival times of swell events. The present analysis suggests that swell analysis will lead to a better representation of extreme surface wind speeds and hence also improve surface wave

models (Cardone et al., 1996; Cavaleri, 2009; Durrant et al., 2013; Feng et al., 2006; P. A. Janssen & Bidlot, 2018; Osinski & Radtke, 2020; Ponce & Ocampo-Torres, 1998; Stopa & Cheung, 2014).

Any moving fetch with nonconstant winds will have spatial wind gradients leading to convergence of wave energy (Section 2.2). A convergence of the characteristic curves from different regions of the moving fetch can create wave-energy hot spots, indicated by crossing characteristic curves (Figure 5). This convergence of wave energy may lead to additional dissipation and/or additional wave-wave interactions, which intensify swell wave growth and the down-shifting of the peak frequency. Hence, it could be modeled as another forcing term in Equation 4, to which the wave spectrum can adjust rather quickly. It also implies that these local wave energy convergences correspond to enhanced breaking, which dissipates part of the wave energy in the upper ocean. Accordingly, we speculate that the location of the strongest winds may not necessarily be the location of the largest momentum transfers to the ocean, nor the location of the observable origin of swell (Figure 4). Instead, swell source locations can be interpreted as markers for intense momentum flux from the wave field to the ocean.

Finally, air-sea fluxes of heat, momentum, and CO_2 are currently parameterized by the standard bulk flux formulae (Edson et al., 2013; Fairall et al., 2003). The wave field's contribution to these fluxes is often described by wave age $\alpha = 2uc_g^{-1}$. We suggest that the sea state at many locations under a moving storm cannot be explained solely by local parameters, like wave age (Figures 5c and 5f; Hsu et al., 2019). Because the local sea state results from the moving wind fetch, its group velocity is constrained by wind forcing to which the wave energy was previously exposed. This introduces a nonlocal condition on the momentum transfer between the atmosphere and ocean. This means that feedbacks between the wave spectrum and the turbulent spectrum of the atmosphere (Ayet et al., 2020; Zou et al., 2020), or feedbacks of surface waves and the upper ocean (Li et al., 2016, 2019), can only capture these wave-induced nonlocal conditions when the wave spectra are computed, that is, advected, rather than assumed by local conditions. Alternatively, the wave spectra could be characterized by metrics that account for nonlocal wave history that goes beyond wave age.

Here, we have used standard wave buoy observations of ocean swell in the eastern Pacific to identify storm systems that generate wave events. We defined a parametric swell model that combines standard swell spectra, a prescribed time decay, and the deep water wave dispersion (Text S1). The novelty in this approach is that swell events from storms are treated as objects whose shapes and origins are learned from the data. This allows us to (a) reevaluate common models of wave spectra, (b) classify and match swell observations in a diverse set of existing data sets, and (c) use deviation from this parametric model to learn about other phenomena, for example, wave-current interaction (Gallet & Young, 2014; Quilfen & Chapron, 2019; Villas Bôas & Young, 2020).

We have outlined how choices in the design of a supervised learning algorithm are linked to the understanding of the physics we wish to investigate. Wave generation is a stochastic process that involves nonlinear physics, such that a single point source of swell is not realistic, even though it is assumed in the parametric model (Section 3.2; Text S1). We account for this paradox by letting the optimization be imprecise (brute-force method), rather than precise (global optimization). The latter would likely overfit the model, which could be corrected by an extensive posterior uncertainty exploration around a prior defined optimum. In either case, imprecise optimization, and uncertainty estimates of the most likely swell origins play an important part in this analysis (Figure 7). This approach suggests that observed swell arrivals could be modeled by a superposition of swell source points using ordinary fetch laws and Green's functions along the trace (Figure 7a, green dots). However, that kind of model would still fall short in describing the nonlinear dynamics prior the linear swell propagation (Section 2).

Appendix A: Solution of the Lagrangian Advection Equation in the (X, t) Plane

A1. Method of Characteristics for Constant Wind Forcing

We follow Kudryavtsev et al. (2015) and solve the advection equation Equation 4 in the moving frame of reference for constant winds u, a constant advection speed V along a characteristic line $(t(s), X(s), c_g(s))$, and with initial conditions $t_0, X(t_0)$ and $c_g(t_0)$ at $s = 0$. The set of equations to be solved is

$$\frac{dt}{ds} = 1 \tag{A1}$$

$$\frac{d\omega_p}{ds} = \left(\frac{g}{u}\right)^2 \phi(\alpha) \tag{A2}$$

$$\frac{dX}{ds} = c_g - V, \tag{A3}$$

where the peak period ω_p is related to the peak group velocity via the deep water dispersion relation $c_g = \frac{1}{2}\frac{g}{\omega_p}$. Equations A1–A3 are solved numerically in Section 2.2 and there after. The characteristics curves are initialized for numerical reason the from $\omega_p \approx 20\,\pi\,\text{s}^{-1}$. This corresponds to c_g of about 7.8×10^{-2} m s^{-1} and its difference from zero has no effects on the overall results.

Equation A1 reduces to $s = t - t_0$ and hence gives the characteristic coordinate as a function of time. Equation A2 is the temporal fetch relation which reads in dimensional coordinates

$$\omega_p(t) = c_{\alpha t}\frac{g}{u}\left(\frac{g}{u}\right)^{q_t}(t - t_0)^{q_t} + C_\omega, \tag{A4}$$

with C_ω is the integration constant, and q_t and c_α are defined in Appendix A3 or Kudryavtsev et al. (2015). Equation A2 can also be solved for the group velocity c_g, and yields

$$c_g(t) = c_\tau^{q_t}\,u\left(\frac{g}{u}\right)^{-q_t}(t - t_0)^{-q_t} + c_g(t_0). \tag{A5}$$

with c_τ again defined in Appendix A3. Finally, the position X along the characteristic reads, from Equation A3

$$X(t) = \frac{1}{-q_t + 1}c_\tau^{q_t}u\left(\frac{g}{u}\right)^{-q_t}(t - t_0)^{-q_t+1} + (t - t_0)[c_g(t_0) - V] + X(t_0). \tag{A6}$$

A2. Derivation of the Critical Time and Length Scale for Constant Moving Wind Forcing

Waves generated at the beginning of the storm ($t_0 = 0$) follow characteristic curves with initial conditions $X(0) = X_0$ and $c_g(0) = 0$, assuming the sea initially at rest.

The time scale t_{crit} at which the trapping of wave every appears is when Equation A5 equals the speed of the storm V, such that

$$V = c_\tau^{q_t}\,u\left(\frac{g}{u}\right)^{-q_t}t_{crit}^{-q_t}, \tag{A7}$$

which yields

$$t_{crit} = \frac{c_\tau}{g}u^{-q}V^{1+\frac{1}{q}}. \tag{A8}$$

At t_{crit}, waves that have started at X_{crit} should be exactly at the rear boundary of the storm, that is, at $X = 0$. From Equation A6, this yields

$$X_{crit} = \frac{-1}{-q_t + 1}c_\tau^{q_t}\,u\left(\frac{g}{u}\right)^{-q_t}t_{crit}^{-q_t+1} + t_{crit}\,V, \tag{A9}$$

$$X_{crit} = \frac{c_\tau}{g}u^{1+\frac{1}{q_t}}V^{1-\frac{1}{q_t}}\left[\frac{q_t}{1 - q_t}\right], \tag{A10}$$

$$X_{crit} = \frac{c_\tau}{g}q\,u^2\left(\frac{u}{V}\right)^{\frac{1}{q}}, \tag{A11}$$

with using Equation A8 and q_t defined in Equation A13. Waves with an initial condition $X_0 > X_{crit}$ will eventually move faster than the storm and will all have the same group velocity at a given time, following the temporal fetch law Equation A5.

A3. Choice of Constants

Wave growth estimated by the Lagrangian advection equation (Equation 4) and subsequent quantities depend on a set of semi-empirical parameters (Badulin et al., 2007). Here we choose parameters based on K. Hasselmann et al. (1976), for the case of a "young sea." With the choice of $q = -3/10$ and a wave growth parameter $c_\alpha = 15.4$, the other parameters follow as

$$p = -5q - \frac{1}{2} = 1, \tag{A12}$$

$$q_t = \frac{q}{1+q} = -0.43, \tag{A13}$$

$$c_{\alpha t} = \left[c_\alpha^{\frac{1}{q}} \frac{1+q}{2} \right]^{q_t} \approx 76.08, \tag{A14}$$

$$c_e \approx 4.41 \times 10^{-7}, \tag{A15}$$

and

$$c_\tau = 2^{\left(1 - \frac{1}{q_t}\right)} c_\alpha^{-\frac{1}{q}} (1+q)^{-1} \approx 1.23 \times 10^5. \tag{A16}$$

Note that, Kudryavtsev et al. (2015) used a slightly different q (see their Appendix A1), but the results are comparable.

Data Availability Statement

The CDIP data are available on the wave buoy observations were furnished by the Coastal Data Information Program (CDIP, https://doi.org/10.18437/C7WC72). The ERA5 reanalysis was provided through the through the Copernicus Climate Change Service Climate Data Store (CDS, https://doi.org/10.24381/cds.adbb2d47) in 2017. Neither the European Commission nor ECMWF is responsible for any use that may be made of the Copernicus information or data it contains. The code is available and preserved at https://doi.org/10.5281/zenodo.5201953.

References

Allen, S., Ferro, C. A. T., & Kwasniok, F. (2020). Recalibrating wind-speed forecasts using regime-dependent ensemble model output statistics. *Quarterly Journal of the Royal Meteorological Society*, *146*, 2576–2596. https://doi.org/10.1002/qj.3806

Andrews, D. G., & McIntyre, M. E. (1976). Planetary waves in horizontal and vertical shear: The generalized Eliassen-Palm relation and the mean zonal acceleration. *Journal of the Atmospheric Sciences*, *33*, 2031–2048. https://doi.org/10.1175/1520-0469(1976)033<2031:pwihav>2.0.co;2

Aouf, L., Hauser, D., Chapron, B., Toffoli, A., Tourain, C., & Peureux, C. (2021). New directional wave satellite observations: Towards improved wave forecasts and climate description in Southern Ocean. *Geophysical Research Letters*, *48*, e2020GL091187. https://doi.org/10.1029/2020GL091187

Arakawa, H. (1954). On the pyramidal, mountainous, and confused sea in the right or dangerous semi-circle of typhoons. *Papers in Meteorology and Geophysics*, *5*, 114–123. https://doi.org/10.2467/mripapers1950.5.2_114

Ardhuin, F., Chapron, B., & Collard, F. (2009). Observation of swell dissipation across oceans. *Geophysical Research Letters*, *36*, L06607. https://doi.org/10.1029/2008GL037030

Ayet, A., Chapron, B., Redelsperger, J. L., Lapeyre, G., & Marié, L. (2020). On the impact of long wind-waves on near-surface turbulence and momentum fluxes. *Boundary-Layer Meteorology*, *174*, 465–491. https://doi.org/10.1007/s10546-019-00492-x

Badulin, S. I., Babanin, A. V., Zakharov, V. E., & Resio, D. (2007). Weakly turbulent laws of wind-wave growth. *Journal of Fluid Mechanics*, *591*, 339–378. https://doi.org/10.1017/S0022112007008282

Barber, N. F., & Ursell, F. (1948). The generation and propagation of ocean waves and swell. I. Wave periods and velocities. *Philosophical Transactions of the Royal Society of London A*, *240*, 527–560. https://doi.org/10.1098/rsta.1948.0005

Behrens, J., Thomas, J., Terrill, E., & Jensen, R. (2019). CDIP: Maintaining a robust and reliable ocean observing buoy network. In *2019 IEEE/OES Twelfth Current, Waves and Turbulence Measurement (CWTM)* (p. 1). San Diego, CA, USA: IEEE. https://doi.org/10.1109/CWTM43797.2019.8955166

Bengtsson, L., Hodges, K. I., & Keenlyside, N. (2009). Will extratropical storms intensify in a warmer climate? *Journal of Climate*, *22*, 2276–2301. https://doi.org/10.1175/2008JCLI2678.1

Bengtsson, L., Hodges, K. I., & Roeckner, E. (2006). Storm tracks and climate change. *Journal of Climate*, *19*, 3518–3543. https://doi.org/10.1175/JCLI3815.1

Bjerknes, J. (1919). On the structure of moving cyclones. *Monthly Weather Review*, *47*, 95–99. https://doi.org/10.1175/1520-0493(1919)47<95:otsomc>2.0.co;2

Bourassa, M. A., Gille, S. T., Bitz, C., Carlson, D., Cerovecki, I., Clayson, C. A., et al. (2013). High-latitude ocean and sea ice surface fluxes: Challenges for climate research. *Bulletin of the American Meteorological Society*, *94*, 403–423. https://doi.org/10.1175/BAMS-D-11-00244.1

Bourassa, M. A., Meissner, T., Cerovecki, I., Chang, P. S., Dong, X., De Chiara, G., et al. (2019). Remotely sensed winds and wind stresses for marine forecasting and ocean modeling. *Frontiers in Marine Science*, *6*. https://doi.org/10.3389/fmars.2019.00443

Bowyer, P. J., & MacAfee, A. W. (2005). The theory of trapped-fetch waves with tropical cyclones—An operational perspective. *Weather Forecast*, *20*, 229–244. https://doi.org/10.1175/WAF849.1

Cardone, V. J., Jensen, R. E., Resio, D. T., Swail, V. R., & Cox, A. T. (1996). Evaluation of contemporary ocean wave models in rare extreme events: The "Halloween Storm" of October 1991 and the "Storm of the Century" of March 1993. *The Journal of Atmospheric and Oceanic Technology*, *13*, 198–230. https://doi.org/10.1175/1520-0426(1996)013<0198:eocowm>2.0.co;2

Catto, J. L. (2018). A new method to objectively classify extratropical cyclones for climate studies: Testing in the Southwest Pacific Region. *Journal of Climate*, *31*, 4683–4704. https://doi.org/10.1175/JCLI-D-17-0746.1

Cavaleri, L. (1994). Applications to wave hindcasting and forecasting; Chapter IV. In *Dynamics and modeling of ocean waves* (p. 532). New York, NY, USA: Cambridge University Press.

Cavaleri, L. (2009). Wave modeling-missing the peaks. *Journal of Physical Oceanography*, *39*, 2757–2778. https://doi.org/10.1175/2009JPO4067.1

(CDS), C. C. C. S. C. D. S. (2017). *Copernicus Climate Change Service (C3S) (2017): ERA5: Fifth generation of ECMWF atmospheric reanalyses of the global climate.*

Chapron, B., Johnsen, H., & Garello, R. (2001). Wave and wind retrieval from sar images of the ocean. *Annales des Telecommunications*, *56*, 682–699. https://doi.org/10.1007/BF02995562

Charney, J. (1947). The dynamics of long waves in a baroclinic westerly current. *Journal of Meteorology*, *4*, 135–162. https://doi.org/10.1175/1520-0469(1947)004<0136:tdolwi>2.0.co;2

Chen, S. S., Price, J. F., Zhao, W., Donelan, M. A., & Walsh, E. J. (2007). The CBLAST-Hurricane program and the next-generation fully coupled atmosphere-wave-ocean models for hurricane research and prediction. *Bulletin of the American Meteorological Society*, *88*, 311–318. https://doi.org/10.1175/bams-88-3-311

Collard, F., Ardhuin, F., & Chapron, B. (2009). Monitoring and analysis of ocean swell fields from space: New methods for routine observations. *Journal of Geophysical Research*, *114*. https://doi.org/10.1029/2008JC005215

Doyle, J. D. (1995). Coupled ocean wave/atmosphere mesoscale model simulations of cyclogenesis. *Tellus*, *47*, 766–778. https://doi.org/10.1034/j.1600-0870.1995.00119.x

Doyle, J. D. (2002). Coupled atmosphere-ocean wave simulations under high wind conditions. *Monthly Weather Review*, *130*, 3087–3099. https://doi.org/10.1175/1520-0493(2002)130<3087:caowsu>2.0.co;2

Durrant, T. H., Greenslade, D. J. M., & Simmonds, I. (2013). The effect of statistical wind corrections on global wave forecasts. *Ocean Modelling*, *70*, 116–131. https://doi.org/10.1016/j.ocemod.2012.10.006

Dysthe, K. B., & Harbitz, A. (1987). Big waves from polar lows? *Tellus*, *39A*, 500–508. https://doi.org/10.1111/j.1600-0870.1987.tb00324.x

Eady, E. T. (1949). Long waves and cyclone waves. *Tellus*, *1*, 33–52. https://doi.org/10.3402/tellusa.v1i3.8507

Edson, J. B., Jampana, V., Weller, R. A., Bigorre, S. P., Plueddemann, A. J., Fairall, C. W., et al. (2013). On the exchange of momentum over the open ocean. *Journal of Physical Oceanography*, *43*, 1589–1610. https://doi.org/10.1175/JPO-D-12-0173.1

Elfouhaily, T., Chapron, B., Katsaros, K., & Vandemark, D. (1997). A unified directional spectrum for long and short wind-driven waves. *Journal of Geophysical Research*, *102*, 15781–15796. https://doi.org/10.1029/97JC00467

Enríquez, A. R., Marcos, M., Álvarez-Ellacuría, A., Orfila, A., & Gomis, D. (2017). Changes in beach shoreline due to sea level rise and waves under climate change scenarios: Application to the Balearic Islands (western Mediterranean). *Natural Hazards and Earth System Sciences*, *17*, 1075–1089. https://doi.org/10.5194/nhess-17-1075-2017

Fairall, C. W., Bradley, E. F., Hare, J. E., Grachev, A. A., & Edson, J. B. (2003). Bulk parameterization of air-sea fluxes: Updates and verification for the COARE algorithm. *Journal of Climate*, *16*, 571–591. https://doi.org/10.1175/1520-0442(2003)016<0571:bpoasf>2.0.co;2

Feng, H., Vandemark, D., Quilfen, Y., Chapron, B., & Beckley, B. (2006). Assessment of wind-forcing impact on a global wind-wave model using the TOPEX altimeter. *Ocean Engineering*, *33*, 1431–1461. https://doi.org/10.1016/j.oceaneng.2005.10.015

Ferreira, O. (2005). Storm groups versus extreme single storms: Predicted erosion and management consequences. *Journal of Coastal Research*, *21*, 221–227.

Gallet, B., & Young, W. R. (2014). Refraction of swell by surface currents. *Journal of Marine Research*, *72*, 105–126. https://doi.org/10.1357/002224014813758959

Gille, S. T. (2005). Statistical characterization of zonal and meridional ocean wind stress. *The Journal of Atmospheric and Oceanic Technology*, *22*, 1353–1372. https://doi.org/10.1175/JTECH1789.1

Hasselmann, K., Barnett, T. P., Bouws, E., Carlson, H., Cartwright, D. E., Enke, K., & Walden, H. (1973). Measurements of wind-wave growth and swell decay during the Joint North Sea Wave Project (JONSWAP). *Ergänzungsheft*, 8–12.

Hasselmann, K., Sell, W., Ross, D. B., & Müller, P. (1976). A parametric wave prediction model. *Journal of Physical Oceanography*, *6*, 200–228. https://doi.org/10.1175/1520-0485(1976)006<0200:apwpm>2.0.co;2

Hasselmann, S., & Hasselmann, K. (1985). Computations and parameterizations of the nonlinear energy transfer in a gravity-wave spectrum. Part I: A new method for efficient computations of the exact nonlinear transfer integral. *Journal of Physical Oceanography*, *15*, 1369–1377. https://doi.org/10.1175/1520-0485(1985)015<1369:capotn>2.0.co;2

Hauser, D., Tourain, C., Hermozo, L., Alraddawi, D., Aouf, L., Chapron, B., & Tran, N. (2020). New observations from the SWIM radar on-board CFOSAT: Instrument validation and ocean wave measurement assessment. *IEEE Transactions on Geoscience and Remote Sensing*, *59*(1). https://doi.org/10.1109/TGRS.2020.2994372

Hell, M. C., Cornuelle, B. D., Gille, S. T., & Lutsko, N. J. (2021). Time-varying empirical probability densities of southern ocean surface winds: Linking the leading mode to SAM and quantifying wind product differences. *Journal of Climate*, *1*, 1–80. https://doi.org/10.1175/JCLI-D-20-0629.1

Hell, M. C., Cornuelle, B. D., Gille, S. T., Miller, A. J., & Bromirski, P. D. (2019). Identifying ocean swell generation events from Ross Ice Shelf seismic data. *The Journal of Atmospheric and Oceanic Technology*, *36*, 2171–2189. https://doi.org/10.1175/JTECH-D-19-0093.1

Hell, M. C., Gille, S. T., Cornuelle, B. D., Miller, A. J., Bromirski, P. D., & Crawford, A. D. (2020). Estimating southern ocean storm positions with seismic observations. *Journal of Geophysical Research: Oceans*, *125*, e2019JC015898. https://doi.org/10.1029/2019JC015898

Hodges, K. I., Lee, R. W., & Bengtsson, L. (2011). A comparison of extratropical cyclones in recent reanalyses ERA-Interim, NASA MERRA, NCEP CFSR, and JRA-25. *Journal of Climate*, *24*, 4888–4906. https://doi.org/10.1175/2011JCLI4097.1

Hoskins, B. J., McIntyre, M. E., & Robertson, A. W. (1985). On the use and significance of isentropic potential vorticity maps. *Quarterly Journal of the Royal Meteorological Society*, *111*, 877–946. https://doi.org/10.1002/qj.49711147002

Hsu, J.-Y., Lien, R.-C., D'Asaro, E. A., & Sanford, T. B. (2019). Scaling of drag coefficients under five tropical cyclones. *Geophysical Research Letters*, *46*, 3349–3358. https://doi.org/10.1029/2018GL081574

Hunt, I. A. (1961). Design of sea-walls and breakwaters. *Transactions of the American Society of Civil Engineers*, *126*, 542–570. https://doi.org/10.1061/taceat.0008347

Husson, R., Ardhuin, F., Collard, F., Chapron, B., & Balanche, A. (2012). Revealing forerunners on Envisat's wave mode ASAR using the Global Seismic Network. *Geophysical Research Letters*, *39*. https://doi.org/10.1029/2012GL052334

Janssen, P. (2004). *The interaction of ocean waves and wind*. Cambridge: Cambridge University Press. https://doi.org/10.1017/CBO9780511525018

Janssen, P. A., & Bidlot, J.-R. (2018). Progress in operational wave forecasting. *Procedia IUTAM*, *26*, 14–29. https://doi.org/10.1016/j.piutam.2018.03.003

Jiang, H., Stopa, J. E., Wang, H., Husson, R., Mouche, A., Chapron, B., & Chen, G. (2016). Tracking the attenuation and nonbreaking dissipation of swells using altimeters. *Journal of Geophysical Research: Oceans*, *121*, 1446–1458. https://doi.org/10.1002/2015JC011536

Kitaigorodskii, S. A. (1962). Applications of the theory of similarity to the analysis of wind-generated wave motion as a stochastic process. *Izv Geophysics Series Academic Science USSR*, *1*, 105–117. https://doi.org/10.1016/0011-7471(62)90050-5

Klotz, B. W., Neuenschwander, A., & Magruder, L. A. (2020). High-resolution ocean wave and wind characteristics determined by the ICE-Sat-2 land surface algorithm. *Geophysical Research Letters*, *47*, e2019GL085907. https://doi.org/10.1029/2019GL085907

Kudryavtsev, V., Golubkin, P., & Chapron, B. (2015). A simplified wave enhancement criterion for moving extreme events. *Journal of Geophysical Research: Oceans*, *120*, 7538–7558. https://doi.org/10.1002/2015JC011284

Kudryavtsev, V., Yurovskaya, M., & Chapron, B. (2021). 2D parametric model for surface wave development under varying wind field in space and time. *Journal of Geophysical Research: Oceans*, *126*, e2020JC016915. https://doi.org/10.1029/2020JC016915

Li, Q., Reichl, B. G., Fox-Kemper, B., Adcroft, A. J., Belcher, S. E., Danabasoglu, G., et al. (2019). Comparing ocean surface boundary vertical mixing schemes including Langmuir turbulence. *Journal of Advances in Modeling Earth Systems*, *11*, 3545–3592. https://doi.org/10.1029/2019MS001810

Li, Q., Webb, A., Fox-Kemper, B., Craig, A., Danabasoglu, G., Large, W. G., & Vertenstein, M. (2016). Langmuir mixing effects on global climate: WAVEWATCH III in CESM. *Ocean Modelling*, *103*, 145–160. https://doi.org/10.1016/j.ocemod.2015.07.020

Makin, V. K. (2008). On the possible impact of a following-swell on the atmospheric boundary layer. *Boundary-Layer Meteorology*, *129*, 469–478. https://doi.org/10.1007/s10546-008-9320-z

Mbengue, C., & Schneider, T. (2016). Storm-track shifts under climate change: Toward a mechanistic understanding using baroclinic mean available potential energy. *Journal of the Atmospheric Sciences*, *74*, 93–110. https://doi.org/10.1175/JAS-D-15-0267.1

Morison, M. L., & Imberger, J. (1992). Water-level oscillations in Esperance Harbour. *Journal of Waterway, Port, Coastal, and Ocean Engineering*, *118*, 352–367. https://doi.org/10.1061/(asce)0733-950x(1992)118:4(352)

Morrow, R., Fu, L.-L., Ardhuin, F., Benkiran, M., Chapron, B., Cosme, E., et al. (2019). Global observations of fine-scale ocean surface topography with the surface water and ocean topography (SWOT) mission. *Frontiers in Marine Science*, *6*. https://doi.org/10.3389/fmars.2019.00232

Munk, W. H. (1947). Tracking storms by forerunners of swell. *Journal of Meteorology*, *4*, 45–57. https://doi.org/10.1175/1520-0469(1947)004<0045:tsbfos>2.0.co;2

Munk, W. H., & Snodgrass, F. E. (1957). Measurements of southern swell at Guadalupe Island. *Deep Sea Research*, *4*(4), 272–286. https://doi.org/10.1016/0146-6313(56)90061-2

Murray, R. J., & Simmonds, I. (1991a). A numerical scheme for tracking cyclone centres from digital data. Part I: Development and operation of the scheme. *Australian Meteorological Magazine*, *39*, 155–166.

Murray, R. J., & Simmonds, I. (1991b). A numerical scheme for tracking cyclone centres from digital data. Part II: Application to January and July general circulation model simulations. *Australian Meteorological Magazine*, *39*, 167–180.

Neiman, P. J., & Shapiro, M. A. (1993). The life cycle of an extratropical marine cyclone. Part I: Frontal-cyclone evolution and thermodynamic air-sea interaction. *Monthly Weather Review*, *121*, 2153–2176. https://doi.org/10.1175/1520-0493(1993)121<2153:tlcoae>2.0.co;2

Neiman, P. J., Shapiro, M. A., & Fedor, L. S. (1993). The life cycle of an extratropical marine cyclone. Part II: Mesoscale structure and diagnostics. *Monthly Weather Review*, *121*, 2177–2199. https://doi.org/10.1175/1520-0493(1993)121<2177:tlcoae>2.0.co;2

Neu, U., Akperov, M. G., Bellenbaum, N., Benestad, R., Blender, R., Caballero, R., et al. (2012). IMILAST: A community effort to intercompare extratropical cyclone detection and tracking algorithms. *Bulletin of the American Meteorological Society*, *94*, 529–547. https://doi.org/10.1175/BAMS-D-11-00154.1

O'Reilly, W. C., Olfe, C. B., Thomas, J., Seymour, R. J., & Guza, R. T. (2016). The California coastal wave monitoring and prediction system. *Coastal Engineering*, *116*, 118–132. https://doi.org/10.1016/j.coastaleng.2016.06.005

Osinski, R. D., & Radtke, H. (2020). Ensemble hindcasting of wind and wave conditions with WRF and WAVEWATCH III driven by ERA5. *Ocean Science*, *16*, 355–371. https://doi.org/10.5194/os-16-355-2020

Pierson, W. J., & Moskowitz, L. (1964). A proposed spectral form for fully developed wind seas based on the similarity theory of S. A. Kitaigorodskii. *Journal of Geophysical Research*, *69*, 5181–5190. https://doi.org/10.1029/JZ069i024p05181

Ponce, S., & Ocampo-Torres, F. J. (1998). Sensitivity of a wave model to wind variability. *Journal of Geophysical Research*, *103*, 3179–3201. https://doi.org/10.1029/97JC02328

Quilfen, Y., & Chapron, B. (2019). Ocean surface wave-current signatures from satellite altimeter measurements. *Geophysical Research Letters*, *46*, 253–261. https://doi.org/10.1029/2018GL081029

Ribal, A., & Young, I. R. (2019). Calibration and cross validation of global ocean wind speed based on scatterometer observations. *The Journal of Atmospheric and Oceanic Technology*, *37*, 279–297. https://doi.org/10.1175/JTECH-D-19-0119.1

Russell, P. E. (1993). Mechanisms for beach erosion during storms. *Continental Shelf Research*, *13*, 1243–1265. https://doi.org/10.1016/0278-4343(93)90051-X

Schemm, S., & Wernli, H. (2014). The linkage between the warm and the cold conveyor belts in an idealized extratropical cyclone. *The Journal of the Atmospheric Sciences*, *71*, 1443–1459. https://doi.org/10.1175/jas-d-13-0177.1

Schultz, D. M., Bosart, L. F., Colle, B. A., Davies, H. C., Dearden, C., Keyser, D., & Winters, A. C. (2018). Extratropical cyclones: A century of research on meteorology's centerpiece. *Meteorological Monographs*, *59*, 16–116. https://doi.org/10.1175/AMSMONOGRAPHS-D-18-0015.1

Schultz, D. M., Keyser, D., & Bosart, L. F. (1998). The effect of large-scale flow on low-level frontal structure and evolution in midlatitude cyclones. *Monthly Weather Review*, *126*, 1767–1791. https://doi.org/10.1175/1520-0493(1998)126<1767:teolsf>2.0.co;2

Shapiro, M. A., & Keyser, D. (1990). Fronts, jet streams, and the tropopause. Extratropical cyclones. In C. W. Newton, & In E. Holopainen (Eds.), The Erik Palmen memorial volume (Vol. 167). Amer Meteor Soc.

Shaw, T. A., Baldwin, M., Barnes, E. A., Caballero, R., Garfinkel, C. I., Hwang, Y.-T., et al. (2016). Storm track processes and the opposing influences of climate change. *Nature Geoscience*, *9*, 656–664. https://doi.org/10.1038/ngeo2783

Sherman, L. (1956). On the wind asymmetry of hurricanes. *The Journal of the Atmospheric Sciences*, *13*, 500–503. https://doi.org/10.1175/1520-0469(1956)013<0500:otwaoh>2.0.co;2

Sinclair, V. A., Rantanen, M., Haapanala, P., Räisänen, J., & Järvinen, H. (2020). The characteristics and structure of extra-tropical cyclones in a warmer climate. *Weather and Climate Dynamics*, *1*, 1–25. https://doi.org/10.5194/wcd-1-1-2020

Snodgrass, F. E., Groves, G. W., Hasselmann, K. F., Miller, G. R., Munk, W. H., & Powers, W. H. (1966). Propagation of ocean swell across the Pacific. *Philosophical Transactions of the Royal Society of London. Series A, Mathematical and Physical Sciences*, *259*, 431–497. https://doi.org/10.1098/rsta.1966.0022

Stopa, J. E., & Cheung, K. F. (2014). Intercomparison of wind and wave data from the ECMWF reanalysis Interim and the NCEP climate forecast system reanalysis. *Ocean Modelling*, *75*, 65–83. https://doi.org/10.1016/j.ocemod.2013.12.006

Tolman, H. L. (2009). User manual and system documentation of WAVEWATCH III TM version 3.14. Tech. Note MMAB Contrib. (Vol. *276*, p. 220).

Trindade, A., Portabella, M., Stoffelen, A., Lin, W., & Verhoef, A. (2020). ERAstar: A high-resolution ocean forcing product. *IEEE Transactions on Geoscience and Remote Sensing*, *58*, 1337–1347. https://doi.org/10.1109/TGRS.2019.2946019

Villas Bôas, A. B., Gille, S. T., Mazloff, M. R., & Cornuelle, B. D. (2017). Characterization of the deep water surface wave variability in the California current region. *Journal of Geophysical Research: Oceans*, *122*, 8753–8769. https://doi.org/10.1002/2017JC013280

Villas Bôas, A. B., & Young, W. R. (2020). Directional diffusion of surface gravity wave action by ocean macroturbulence. *Journal of Fluid Mechanics*, *890*. https://doi.org/10.1017/jfm.2020.116

Wentz, F. J., Scott, R., Hoffman, R., Leidner, S. M., Atlas, R., & Ardizzone, J. (2015*). Remote sensing systems cross-calibrated multi-platform (CCMP) 6-hourly ocean vector wind analysis product on 0.25 deg grid, version 2.0*. Santa Rosa, CA: Remote Sensing Systems. Retrieved from www.remss.com/measurements/ccmp

Wilson, B. (1957). Origin and effects of long period wave in ports. Proceedings of 19th International Navig Congress Section II Communication I, (pp. 13–61).

Young, I. R. (1988). Parametric hurricane wave prediction model. *Journal of Waterway, Port, Coastal, and Ocean Engineering*, *114*, 637–652. https://doi.org/10.1061/(asce)0733-950x(1988)114:5(637)

Young, I. R. (2003). A review of the sea state generated by hurricanes. *Marine Structures*, *16*, 201–218. https://doi.org/10.1016/S0951-8339(02)00054-0

Young, I. R., Hasselmann, S., & Hasselmann, K. (1987). Computations of the response of a wave spectrum to a sudden change in wind direction. *Journal of Physical Oceanography*, *17*, 1317–1338. https://doi.org/10.1175/1520-0485(1987)017<1317:cotroa>2.0.co;2

Young, I. R., & Vinoth, J. (2013). An "extended fetch" model for the spatial distribution of tropical cyclone wind–waves as observed by altimeter. *Ocean Engineering*, *70*, 14–24. https://doi.org/10.1016/j.oceaneng.2013.05.015

Zakharov, V. E., & Badulin, S. I. (2011). On energy balance in wind-driven seas. *Doklady Earth Sciences*, *440*, 1440–1444. https://doi.org/10.1134/S1028334X11100175

Zakharov, V. E., Badulin, S. I., Geogjaev, V. V., & Pushkarev, A. N. (2019). Weak-turbulent theory of wind-driven sea. *Earth and Space Science*, *6*, 540–556. https://doi.org/10.1029/2018EA000471

Zou, Z., Li, S., Huang, J., Li, P., Song, J., Zhang, J. A., & Wan, Z. (2020). Atmospheric boundary layer turbulence in the presence of swell: Turbulent kinetic energy budget, Monin-Obukhov similarity theory, and inertial dissipation method. *Journal of Physical Oceanography*, *50*, 1213–1225. https://doi.org/10.1175/JPO-D-19-0136.1